

1 **Interpretable Machine Learning Quantifies Composition and Size**

2 **Influences~~Controls~~ on Aerosol Spectral Absorption**

3
4 **Wenfang Wang¹, Pengfei Tian^{1,2*}, Shuhua Zeng¹, Yifei Zhang¹, Zeren Yu¹, Chen**
5 **Cui¹, Yunfei Wu³, Min Chen^{1*}, Lei Zhang^{1,2}**

6 ¹ Key Laboratory for Semi-Arid Climate Change of the Ministry of Education, College
7 of Atmospheric Sciences, Lanzhou University, Lanzhou 730000, China.

8 ² Collaborative Innovation Center for Western Ecological Safety, Lanzhou University,
9 Lanzhou 730000, China.

10 ³ State Key Laboratory of Atmospheric Environment and Extreme Meteorology,
11 Institute of Atmospheric Physics, Chinese Academy of Sciences, Beijing 100029,
12 China.

13 Corresponding author: P. Tian (tianpf@lzu.edu.cn) and M. Chen (chenmin@lzu.edu.cn)

14

15 **Abstract**

16 The spectral dependence of aerosol absorption, characterized by the absorption
17 Ångström exponent (AAE), strongly influences radiative effects, yet the relative
18 importance of controlling factors remains poorly quantified. We integrate multisource
19 observations with an interpretable machine-learning framework (Shapley Additive
20 Explanations, SHAP) to disentangle the roles of chemical composition and particle size
21 in ~~shaping~~ predicting AAE and to evaluate radiative impacts. Field observation in
22 Beijing reveal that near-surface AAE is predominantly influenced by higher fine
23 mineral dust and water-soluble inorganic ions fractions. Multi-year columnar data
24 identify dust loading as the dominant ~~factor~~ predictor, followed by carbonaceous
25 aerosols. The fine-mode radius accounts for 29% of size parameters cumulative
26 importance and ranks closely with black carbon. SHAP diagnostics highlight that
27 columnar AAE contributes to radiative forcing at the top of the atmosphere (TOA)
28 comparably to single scattering albedo (SSA), while its impact is clearly weaker at the
29 bottom of the atmosphere and in the atmosphere. These findings help clarify AAE
30 determinants and reduce uncertainties in aerosol radiative effect assessments.

31

32 1 Introduction

33 Light-absorbing aerosols (LAAs), primarily black carbon (BC), brown carbon
34 (BrC), and mineral dust, significantly influence regional and global climate by
35 absorbing solar radiation (Bahadur et al., 2012; Cappa et al., 2016; Kok et al., 2017;
36 Nishant et al., 2019). For instance, BC contributed a net positive effective radiative
37 forcing of $0.11 \text{ W}\cdot\text{m}^{-2}$ during 1750–2019, with a wide uncertainty range from -0.20 to
38 $+0.42 \text{ W}\cdot\text{m}^{-2}$ (Intergovernmental Panel On Climate Change (Ipcc), 2023), reflecting
39 limited observational constraints on aerosol optical/microphysical properties and their
40 inaccurate representation in models (Gliß et al., 2021; Lee et al., 2016). A practical
41 diagnostic for the spectral shape of absorption is the Absorption Ångström Exponent
42 (AAE) (Ångström, 1929; Lewis et al., 2008). For pure BC, AAE is theoretically close
43 to 1.0, but observations show a range of 0.6–1.6 (Kirchstetter et al., 2004; Lack and
44 Cappa, 2010; Gyawali et al., 2012; Chakrabarty et al., 2013; Wang et al., 2021). BrC
45 and mineral dust exhibit relatively stronger absorption in the ultraviolet and visible
46 spectral wavelengths, typically yielding AAE values greater than 2.0 (Russell et al.,
47 2010; Park et al., 2018; Zhang et al., 2020; Cuesta-Mosquera et al., 2024). For example,
48 BrC AAE is frequently reported to be ~2–6 depending on source and aging, whereas
49 dust AAE is typically ~2–4 owing to shortwave absorption by iron oxides (Bergstrom
50 et al., 2007). Because AAE encodes source and process information that governs
51 aerosol absorption from ultraviolet to the near-infrared wavelength range, tighter

52 constraints on AAE can help reduce uncertainties in aerosol radiative effects (Cazorla
53 et al., 2013; Lack and Langridge, 2013; Sand et al., 2021).

54 AAE has been characterized using multiple observational approaches, including
55 in situ multi-wavelength absorption measurements and surface-based remote sensing
56 retrievals (Li et al., 2022). In situ observations provide high-precision, process-
57 resolving constraints on aerosol absorption spectra near the surface and therefore serve
58 as an important benchmark for evaluating remote sensing products and model
59 simulations (Gliß et al., 2021). In contrast, surface-based remote sensing can retrieve
60 aerosol properties integrated over the entire atmospheric column, such as Aerosol
61 Robotic Network (AERONET), enabling a broader view of aerosol spectral absorption
62 and its radiative properties (Dubovik and King, 2000). Combining in situ and column
63 retrievals is particularly valuable because they constrain complementary aspects of
64 aerosol spectral absorption. In situ measurements are sensitive to near-surface processes
65 (emissions, hygroscopic growth and aging) but have limited spatial and vertical
66 representativeness, whereas AERONET provides column-averaged constraints that are
67 directly connected to radiative impacts but can be influenced by vertical layering and
68 retrieval assumptions (Li et al., 2022). Therefore, integrating near-surface with
69 columnar AAE enables us to provide improved observational guidance for models, and
70 better constrain column characteristics relevant to radiative forcing.

71 Both near-surface and columnar AAE ~~varies~~-vary with particle size distribution,
72 chemical composition, and mixing state- (Russell et al., 2010; Scarnato et al., 2013;

73 Li et al., 2016; Schuster et al., 2016a; Sotiropoulou et al., 2025). For instance, [near-](#)
74 [surface BC](#) AAE may decrease as BC cores grow or as aggregates become more
75 compact during aging processes (Liu et al., 2018). Recent numerical simulation further
76 indicates that secondary organic coatings can increase [near-surface](#) AAE, with
77 sensitivity to coating thickness (Zhang et al., 2025). In contrast, photochemical
78 bleaching lowers BrC ultraviolet absorption and [near-surface](#) AAE (Wang et al., 2019;
79 [Li et al., 2025](#)). [Russell et al., \(2010\) showed that columnar AAE values are strongly](#)
80 [correlated with aerosol composition or type.](#) Heterogeneous aging of long-range-
81 transported dust may enhance absorption, also affecting [columnar](#) AAE (Tian et al.,
82 2018). The magnitudes and signs of these effects depend on location, season, and
83 processing history, complicating both measurements and modeling and propagating to
84 radiative forcing uncertainty (Sand et al., 2021; Li et al., 2022; Ponczek et al., 2022).

85 Studying the impact of individual factors on AAE is relatively straightforward.
86 Previous studies have already examined the effects of particle size, chemical
87 composition, and mixing state on AAE in isolation (Wu et al., 2015; Schuster et al.,
88 2016b; Li et al., 2024). However, quantitatively attributing the relative contributions of
89 particle size and chemical composition to AAE remains a challenging task due to
90 nonlinearity and collinearity among predictors. For example, observations show that
91 composition appears dominant when the shape of size distribution is quasi-stationary
92 (Utry et al., 2014), whereas Mie-theory studies highlight the role of the imaginary
93 refractive index of organics over size in explaining absorption changes (Yang et al.,

94 2025). Although these studies effectively highlight the roles of particle size and
95 chemical composition, they lack quantitative assessments of their relative importance.

96 The Shapley Additive exPlanations (SHAP) method offers a principled framework
97 for feature attribution in machine learning predictions and has been widely adopted in
98 atmospheric sciences, such as boundary-layer height inversion, ozone formation and
99 cloud-condensation-nuclei studies (Peng et al., 2023; Tao et al., 2024; Wang et al.,
100 2025a). SHAP analysis has also been applied to aerosol absorption studies to precisely
101 quantify the relative contribution of various chromophores to BrC absorption,
102 providing a mechanistic understanding of its key drivers (Wang et al., 2024). Its
103 potential to predict AAE and quantify the relative contributions of individual factors
104 remains unexplored. Addressing this gap would offer an interpretable, data-driven
105 perspective on aerosol spectral absorption.

106 This study aims to quantify the relative importance of chemical composition and
107 particle size influencing AAE using surface observations together with long-term
108 AERONET column retrievals over Beijing. We apply multiple linear regression to
109 identify their influence on near-surface AAE. Subsequently, we train an ensemble of
110 machine-learning models to predict columnar AAE. The best-performing model
111 (CatBoost) is selected for the final prediction, as described later in Section 2.4. Then
112 SHAP is used for interpretative analysis to quantify the contributions of different
113 columnar aerosol physical and chemical parameters. Finally, we also evaluate the
114 diagnostic power of columnar AAE for radiative effects, including aerosol direct

115 ~~radiative forcing (ADRF) and radiative forcing efficiency (ARFE) using interpretable~~
116 ~~machine-learning framework, and to elucidate the critical role of AAE in radiative~~
117 ~~effects. We applied machine learning methods for columnar AAE (AAE_{col}), and~~
118 ~~assessed how AAE_{col} influences aerosol direct radiative forcing (ADRF) and aerosol~~
119 ~~radiative forcing efficiency (ARFE). During the modeling process, an ensemble of~~
120 ~~models was initially trained, after which the optimal model was selected to predict~~
121 ~~AAE_{col} , ADRF, and ARFE, with the SHAP algorithm used for interpretative analysis.~~

122 **2 Methods**

123 **2.1 Field Campaign and Data Processing**

124 An intensive observation campaign focusing on aerosol properties was conducted
125 in urban Beijing, China, from 16 December 2023 to 15 January 2024. Online and offline
126 instruments were deployed on the rooftop of the Institute of Atmospheric Physics,
127 Chinese Academy of Sciences (Building #3; 39.98°N, 116.39°E), approximately 45 m
128 above ground level. All online instruments were housed in a temperature-controlled
129 room maintained at ~20 °C to ensure measurement stability, and sampling lines were
130 equipped with Nafion dryers to minimize the influence of ambient humidity.

131 **2.1.1 In Situ Online Aerosol Observations**

132 Aerosol absorption coefficients ($b_{abs,\lambda}$) at 375, 532, and 870 nm were measured
133 using photoacoustic extincionimeters (PAX, DMT Inc., USA). The PAX measures

134 aerosol light absorption using the photoacoustic technique, in which absorbed laser
135 energy is converted into periodic heating of the surrounding gas, generating an acoustic
136 pressure wave in an acoustic resonator that is detected by a sensitive microphone (Truex
137 and Anderson, 1979). The light absorption ($b_{abs,pax}$) can be calculated as:

$$138 \quad b_{abs,pax} = \frac{P_{mic} \times A_{res} \times \pi^2 \times f_{res}}{P_L \times (\gamma - 1) \times Q} \quad (1)$$

139 where P_{mic} and P_L are the pressure of the microphone and the laser power,
140 respectively; A_{res} , f_{res} and Q indicate the cross-sectional area, resonance frequency,
141 and quality factor of the resonator; γ is the isobaric and isosteric specific heat ratio.
142 Then the $b_{abs,\lambda}$ is obtained by subtracting the background absorption measured with
143 particle-free air from $b_{abs,pax}$. In addition, the PAX measures aerosol scattering with
144 an integrated wide-angle reciprocal nephelometer.

145 Prior to deployment, each PAX was calibrated following the procedure described
146 in Wu et al., 2015: (i) the scattering channel was calibrated using high-concentration
147 ammonium sulfate aerosol by regressing the extinction coefficient (b_{ext}) derived from
148 laser power attenuation against the instrument-recorded scattering coefficient (b_{sca}).
149 The scattering calibration factor was then adjusted by applying the regression slope as
150 a multiplicative correction; (ii) the absorption channel was calibrated using high-
151 concentration Aquadag aerosol by regressing ($b_{ext} - b_{sca}$) against the instrument-
152 recorded photoacoustic absorption. The absorption calibration factor was then updated
153 by dividing it by the regression slope.

154 The near-surface aerosol absorption Ångström exponent (AAE_{sfc}) was calculated

155 as:

$$156 \quad AAE_{sfc} = -\frac{\log(b_{abs,\lambda_1}) - \log(b_{abs,\lambda_2})}{\log(\lambda_1) - \log(\lambda_2)} \quad (2)$$

157 where $\lambda_1 = 375$ nm, $\lambda_2 = 870$ nm. Hourly $PM_{2.5}$ (particle matters with an aerodynamic
158 diameter ≤ 2.5 μm) mass concentrations were obtained from the China National
159 Environmental Monitoring Network for the Beijing urban site. These datasets were
160 used to calculate mass absorption efficiency (MAE) of $PM_{2.5}$:

$$161 \quad MAE_{\lambda} = \frac{b_{abs,\lambda}}{PM_{2.5}} \quad (3)$$

162 Size distributions were measured with a scanning mobility particle sizer (SMPS,
163 Model 3082, TSI Inc., 8.8–310.6 nm, Stokes diameter) and an aerodynamic particle
164 sizer (APS, Model 3321, TSI Inc., 0.54–19.8 μm , aerodynamic diameter), with SMPS
165 data converted to aerodynamic diameter (Text S1) (Shang et al., 2018). To ensure
166 measurement accuracy, the flow systems of the SMPS and APS were periodically
167 checked and calibrated by the manufacturer (TSI Inc.) through regular return-service
168 calibration. In addition, hourly meteorological parameters (wind speed and direction,
169 temperature, and relative humidity) were obtained from the 47 m meteorological tower
170 at the Institute of Atmospheric Physics.

171 **2.1.2 Offline Aerosol Sampling**

172 Offline $PM_{2.5}$ samples were collected on quartz-fiber filters (90 mm diameter;
173 Whatman 1855-090). Prior to sampling, quartz-fiber filters were pre-cleaned to
174 minimize filter background. Briefly, filter cassettes were rinsed with absolute ethanol

175 and air-dried, and aluminum-foil liners cut to the filter size were pre-baked at 550 °C
176 for 3 h to remove residual carbon. The quartz filters were sequentially soaked in
177 ultrapure water (5 min × 3 cycles, followed by 2 h × 2 cycles), oven-dried at 150 °C for
178 1 h, and then prebaked at 550 °C for 5 h to reduce the influence of adsorbed organic
179 and inorganic materials. After cooling, the filters were wrapped in prebaked aluminum
180 foil and conditioned for 48 h in a constant temperature and humidity environment prior
181 to gravimetric determination. Then the pre-sampling filter mass was measured using an
182 electronic microbalance (BSA124S-CW, Sartorius; readability ±0.1 mg). Sampling was
183 conducted using a medium-volume air sampler (Model 2030, Laoshan Electronic
184 Instrument Co., Ltd.) operated at 100 L·min⁻¹ and equipped with a PM_{2.5} inlet. The inlet
185 was installed at approximately 2 m above ground level. Daytime samples were collected
186 from 09:00 to 20:30, and nighttime samples from 21:00 to 08:30 the following day.

187 After sampling, all filters were analyzed for major chemical compositions,
188 including water-soluble inorganic ions (Na⁺, K⁺, NH₄⁺, Ca²⁺, Mg²⁺, Cl⁻, NO₃⁻, and SO₄²⁻)
189 measured by ion chromatography (881 Compact IC Pro, Metrohm; and ICS-1500,
190 Dionex Inc.), metallic elements (Al, Ca, Mg, Fe, and Ti) determined by inductively
191 coupled plasma–atomic emission spectrometry (ICP-AES; iCAP 7400, Thermo), and
192 organic carbon (OC), and elemental carbon (EC) quantified using the thermal/optical
193 carbon analyzer (DRI Model 2015, USA) based on the thermal/optical reflectance
194 (TOR) method (Chow et al., 2007). The chemical analysis process is described in detail
195 in Supplementary Text S2.

196 PM_{2.5} was reconstructed as the sum of organic matter (OM=1.6×OC) (Guinot et
 197 al., 2007), EC, non-dust water-soluble ions (nd-WSII, and fine mineral dust (FMD)
 198 derived from crustal elements (Malm et al., 1994; Tian et al., 2023), showing good
 199 agreement with measured PM_{2.5} (r = 0.82). Here, nd-WSII was defined as the sum of
 200 K⁺, NH₄⁺, NO₃⁻, and SO₄²⁻, while Na⁺, Ca²⁺, Mg²⁺, and Cl⁻ were excluded. Ca²⁺ and
 201 Mg²⁺ were treated as dust-related species, Na⁺ was excluded due to generally elevated
 202 blanks associated with quartz-fiber filters and glassware, and Cl⁻ was excluded given
 203 its strong association with Mg²⁺ (r = 0.77, Table S1). The FMD was defined as follows:

$$204 \quad [FMD] = 2.20[Al] + 2.49[Si] + 1.63[Ca] + 2.42[Fe] + 1.94[Ti] \quad (4)$$

205 where [Si] = 1.5 [Al].

206 2.2 Multiple Linear Regression

207 The influence of particle size and chemical composition on AAE_{sfc} was assessed
 208 using a standardized multiple linear regression:

$$209 \quad \widehat{AAE}_{sfc} = a + b \times \widehat{FMD} + c \times \widehat{nd-WSII} + d \times \widehat{D_{SMPS}} + e \times \widehat{D_{APS}} \quad (5)$$

210 where \widehat{AAE}_{sfc} denotes the standardized AAE_{sfc}; a represents the intercept term, any
 211 remaining influence not parameterized by the selected predictors is captured by the
 212 intercept term encompassing EC, OM, and other potential influencing factors not
 213 explicitly accounted for; b , c , d , and e are regression coefficients; \widehat{FMD} ,
 214 $\widehat{nd-WSII}$, $\widehat{D_{SMPS}}$, and $\widehat{D_{APS}}$ are standardized variables of FMD fraction, nd-WSII
 215 fraction, and mean diameters from SMPS and APS, respectively. To ensure consistent
 216 temporal support between offline chemistry and online optical measurements, we

217 aggregate AAE_{sfc} (and size-related parameters) over the same sampling windows and
218 use these window-mean values. We note that AAE_{sfc} can vary within a given sampling
219 period; however, such within-period variability is not resolvable by the integrated filter
220 chemistry and therefore cannot be explicitly attributed at finer temporal resolution. To
221 transparently characterize the associated representativeness uncertainty, we quantify
222 the within-window dispersion of AAE_{sfc} using the standard deviation across all
223 sampling windows and provide its frequency and cumulative distributions (Fig. S2). In
224 particular, ~ 90% of the sampling periods show a standard deviation no greater than
225 0.35. This result indicates that window-mean AAE_{sfc} provides a reasonable
226 representative value at the filter timescale. ~~Offline chemical composition data were~~
227 ~~temporally matched to the corresponding online measurements based on sampling~~
228 ~~periods.~~ Due to power outage on 27 December 2023 and 3 January 2024, daytime data
229 for 27 December and both daytime and nighttime data for 3 January were unavailable.
230 In future studies, higher-time-resolution measurements of aerosol chemical
231 composition would be valuable for more directly linking short-timescale composition
232 variability with AAE.

233 Notably, to further evaluate the robustness of the regression coefficients, we
234 conducted a nonparametric bootstrap analysis with 1000 resamples. We also tested an
235 extended model including EC and OM fractions as additional predictors. However, the
236 extended model yielded highly unstable coefficient estimates under bootstrap
237 resampling, with strong dispersion and frequent sign changes (Table S1). In contrast,

238 the reduced model provides stable and physically interpretable coefficients for the key
239 predictors and demonstrates good predictive skill for AAE_{sfc} (the coefficient of
240 determination (R^2) = 0.75, root mean square error (RMSE) = 0.13, mean absolute error
241 (MAE) = 0.10; Table S2). Consistent with these robustness results, our correlation
242 analysis further indicates that EC and OM fractions are not significantly associated with
243 AAE_{sfc} during this campaign (Section 3.2). Therefore, we retained the parsimonious
244 formulation without EC and OM fractions for subsequent analyses (Equation (5)).

245

246 **2.3 AERONET Data**

247 We used data from the Beijing Aerosol Robotic Network (AERONET) site (39.98°
248 N, 116.38° E). Level 2.0 quality-assured Version 3 inversion products were selected.
249 Key parameters include aerosol absorption optical depth (AAOD) at 440, 675, 870, and
250 1020 nm to calculate columnar AAE (AAE_{col}):

$$251 \quad AAOD_{\lambda} = k \times \lambda^{-AAE_{col}} \quad (6)$$

252 where k is a constant. In addition, aerosol size-related parameters were obtained,
253 including volume size distributions for radii in the 0.05–15.00 μm range, mean radii of
254 fine-mode and coarse-mode particles (R_{fine} , R_{coarse}), as well as volume concentrations
255 of fine-mode (0.05–0.60 μm , vol_{fine}) (Dubovik et al., 2002) ~~–(Sinyuk et al., 2020)~~ and
256 total particles (vol_{total}). The fine-mode fraction (FMF) was then calculated as:

$$257 \quad FMF = \frac{vol_{fine}}{vol_{total}} \quad (7)$$

258 To investigate the influence of chemical composition on AAE_{col} , we used the

259 chemical composition dataset derived from AERONET inversions (Zhang et al., 2024),
260 including black carbon (BC), brown carbon (BrC), coarse-mode absorbing insoluble
261 matter (CAI, representing coarse absorbing dust), coarse-mode non-absorbing insoluble
262 matter (CNAI, representing coarse non-absorbing dust and aged carbonaceous aerosols),
263 and fine-mode non-absorbing insoluble matter (FNAI, representing fine non-absorbing
264 dust and organic carbon) (Li et al., 2019; Zhang et al., 2024).

265 Notably, the column chemical components (BC, BrC, CAI, CNAI, and FNAI) used
266 here are retrieval-based and should not be interpreted as directly measured chemical
267 mas. They are inferred from spectral Sun–sky photometer observations through the
268 AERONET inversion (which retrieves column-integrated size distribution and complex
269 refractive index from AOD and sky radiances) and a subsequent component-mixing
270 framework (GRASP/Component) that maps the retrieved optical constraints to
271 optically equivalent component fractions (Dubovik et al., 2000; Sinyuk et al., 2020; Li
272 et al., 2019). In doing so, the component retrieval necessarily relies on prescribed
273 assumptions, notably fixed complex refractive indices for the dry components, an
274 internal-mixing rule (commonly Maxwell–Garnett effective medium approximation) to
275 compute effective optical properties, and constraints on how absorbing components are
276 partitioned between fine and coarse modes (Li et al., 2019). For dust, non-sphericity is
277 treated using spheroid-based scattering models rather than purely spherical Mie theory
278 (Dubovik et al., 2006).

279 These assumptions introduce additional uncertainty beyond the base AERONET

280 inversion. As background, absorption-related AERONET inversion products (e.g.,
281 SSA/AAOD) are substantially less stable at low aerosol loading; under favorable
282 loading conditions, SSA uncertainty is typically on the order of ~0.03, while it increases
283 rapidly as AOD decreases (Dubovik et al., 2000; Sinyuk et al., 2020). Component
284 volume fractions inherit this sensitivity and, in addition, respond to uncertainties in
285 prescribed component optics and mixing rules. Sensitivity tests in the
286 GRASP/Component literature indicate that, for $AOD_{440} \geq 0.4$ and sufficiently non-
287 negligible component fractions, the uncertainty in retrieved BC, CAI, FNAI, and CNAI
288 volume fractions is commonly within ~50%, whereas BrC generally remains more
289 uncertain at low BrC fractions but can approach the ~50% level when BrC becomes a
290 substantial contributor (Li et al., 2019). Nevertheless, this approach has been applied
291 by Zhang et al. (2022) and Zhang et al. (2024), who obtained reliable aerosol chemical-
292 component information from remote-sensing measurements. To reduce the low-loading
293 regime where absorption and component retrievals are most uncertain, we restricted our
294 analysis to $AOD_{440} > 0.4$.

295 To further assess the radiative impacts of aerosols, we also employed AERONET
296 shortwave instantaneous aerosol direct radiative forcing (ADRF) and aerosol radiative
297 forcing efficiency (ARFE) data, where ARFE is defined as ADRF per unit aerosol
298 optical depth (AOD) at 550 nm, reported at the top of the atmosphere (TOA), bottom
299 of the atmosphere (BOA), and in the atmosphere (ATM) (Holben et al., 1998). These
300 radiative quantities are computed within the AERONET inversion radiative-transfer

301 module under cloud-free conditions, using AERONET-retrieved aerosol optical
302 properties and surface albedo as inputs. ADRF is defined as the difference in broadband
303 shortwave radiative fluxes between aerosol-free and aerosol-laden conditions (García
304 et al., 2008):

$$305 \quad ADRF_{TOA} = F_{0,TOA}^{\uparrow} - F_{TOA}^{\uparrow} \quad (8)$$

$$306 \quad ADRF_{BOA} = F_{BOA}^{\downarrow} - F_{0,BOA}^{\downarrow} \quad (9)$$

$$307 \quad ADRF_{ATM} = ADRF_{TOA} - ADRF_{BOA} \quad (10)$$

308 where F and F₀ denote radiative fluxes with and without aerosols, and arrows indicate
309 upward or downward fluxes. ARFE is defined as radiative forcing per unit aerosol
310 optical depth:

$$311 \quad ARFE = \frac{ADRF}{AOD_{550}} \quad (11)$$

312 where AOD₅₅₀ is the AOD at 550 nm. Defined this way, negative ADRF and ARFE
313 indicate shortwave cooling.

314 **2.4 Shapley Additive Explanations (SHAP)**

315 To quantify how particle size and chemical composition control the AAE_{col}, we
316 trained and compared three ensemble tree-based regressors: Extreme Gradient
317 Boosting (XGBoost), Random Forest (RF), and Categorical Boosting (CatBoost). Each
318 model was trained using seven predictor variables, including five chemical
319 compositions (BrC, BC, CAI, CNAI, and FNAI), and four size parameters (R_{fine}, R_{coarse},
320 vol_{fine}, and volume concentrations of ~~coarse~~coarse-mode (vol_{coarse})).

321 Model performance was evaluated using a consistent training-testing split (80%

322 ~~of dataset were used for the training set, and 20% were used for the test set) and~~
323 ~~quantified by the coefficient of determination (R^2), root-mean-square error (RMSE),~~
324 ~~and mean absolute error (MAE). The CatBoost model in our case was subsequently~~
325 ~~adopted for further interpretation (Fig. S7). The RF model achieved an R^2 of 0.58, an~~
326 ~~RMSE of 0.43, and an MAE of 0.30. In comparison, the CatBoost model yielded an R^2~~
327 ~~of 0.64, an RMSE of 0.40, and an MAE of 0.29, while the XGBoost model showed an~~
328 ~~R^2 of 0.64, an RMSE of 0.40, and an MAE of 0.30 (Fig. S3). The CatBoost model in~~
329 ~~our case was subsequently adopted for further interpretation. Furthermore, the SHapley~~
330 ~~Additive exPlanations (SHAP) analysis was applied to decompose the model output~~
331 ~~into additive feature contributions, enabling quantitative assessment of the relative~~
332 ~~contribution and sensitivity of individual aerosol composition and size parameters in~~
333 ~~predicting/determining. Predicted versus observed diagnostics are shown in~~
334 ~~Supplementary Fig. S7.~~

335 Similarly, to evaluate aerosol radiative impacts, XGBoost, RF, and CatBoost
336 models also were trained using distinct predictor sets for different radiative metrics.
337 The AERONET ADRF and ARFE products are generated by a radiative-transfer
338 calculation (Section 2.4); therefore, our goal is not to replace radiative transfer. Here
339 machine-learning model is used to quantify the relative importance of AAE_{col} as a
340 predictor of ADRF and ARFE variability, rather than implying a causal pathway where
341 AAE_{col} independently drives ADRF and ARFE.

342 For ~~aerosol direct radiative forcing (ADRF)~~, five optical properties (AOD,

343 single scattering albedo (SSA), asymmetry parameter (g), surface albedo (SA), and
 344 AAE_{col}) were used as inputs. For ~~radiative forcing efficiency (ARFE)~~, the target
 345 definition (ARFE = ADRF/AOD) was kept unchanged; however, AOD was included
 346 during model fitting together with SSA, g, SA, and AAE_{col} so that the models could
 347 learn any residual nonlinearity and interactions involving AOD. Performance was again
 348 evaluated using a consistent training-testing split, with 80% of the dataset used for
 349 training and the remaining 20% for testing. The evaluation was quantified by R², RMSE,
 350 and MAE. The performance metrics for the three models are summarized in Fig. S4-
 351 S5. Performance was again quantified by R², RMSE, and MAE on a consistent split.
 352 CatBoost in our case was retained as the best-performing model across TOA, BOA, and
 353 ATM, as it showed the highest or near-highest R² together with the lowest or near-
 354 lowest RMSE and MAE among the tested models. R², RMSE, and MAE are defined as
 355 follows:

$$356 \quad R^2 = 1 - \frac{\sum_{i=1}^n (y_i - \hat{y}_i)^2}{\sum_{i=1}^n (y_i - \bar{y})^2} \quad (12)$$

$$357 \quad RMSE = \sqrt{\frac{1}{n} \sum_{i=1}^n (y_i - \hat{y}_i)^2} \quad (13)$$

$$358 \quad MAE = \frac{1}{n} \sum_{i=1}^n |y_i - \hat{y}_i| \quad (14)$$

359 where n represents the number of input samples. y_i and \hat{y}_i are the observed and
 360 predicted values, respectively; \bar{y} refers to the mean of the target values predicted by
 361 the model. In this study, y corresponds to the target variable, including AAE_{sfc} (Section
 362 2.2), AAE_{col}, ADRF, and ARFE in this Section. Predicted and observed comparisons are

363 ~~provided in Supplementary Fig. S8-S9.~~

364 To attribute ARFE variations while controlling for AOD, we employed SHAP with
365 a scenario-based conditioning approach. Specifically, we recomputed SHAP values on
366 the held-out test set after fixing AOD to four levels (25th, 50th, 75th percentiles, and
367 mean), computed from the training set to avoid information leakage, while leaving all
368 other predictors unchanged. This yields SHAP attributions for SSA, g, SA, and AAE_{col}
369 conditional on AOD at representative states. (The 50th percentile case is shown in the
370 main text, others in Supplementary). For ADRF, SHAP was computed in the standard
371 manner using all five predictors (AOD, SSA, g, SA, AAE) without conditioning.

372

带格式的：缩进：首行缩进： 0 字符

373 **3 Results and Discussion**

374 **3.1 Aerosol Characteristics During the Field Campaign**

375 Figure 1 provides the near-surface AAE (AAE_{sfc}) variability and its co-variation
376 with $PM_{2.5}$ composition and particle size during the Beijing campaign. In Fig. 1a, the
377 stacked bars show the window-resolved $PM_{2.5}$ mass fractions of non-dust water-soluble
378 ions (nd-WSII), fine mineral dust (FMD), organic matter (OM), and elemental carbon
379 (EC), overlaid with AAE_{sfc} and the mean particle diameters derived from the fine-mode
380 (SMPS) and coarse-mode (APS) measurements. Notably, periods with elevated FMD
381 fractions generally coincide with higher AAE_{sfc} , whereas intervals dominated by nd-
382 WSII tend to correspond to lower AAE_{sfc} , consistent with dust-related enhancement of

383 short-wavelength absorption. These co-variations motivate the quantitative attribution
384 in Section 3.2, where we assess how the fractions of FMD and nd-WSII relate to the
385 observed spectral absorption dependence.

386 ~~During the campaign, aerosol absorption decreased systematically with~~
387 ~~wavelength (375, 532, and 870 nm) (Fig. S2d), demonstrating typical wavelength-~~
388 ~~dependent characteristics. The corresponding mass absorption efficiencies were~~
389 ~~relatively low (0.49 ± 0.24 , 0.21 ± 0.08 , and 0.12 ± 0.04 m^2g^{-1}), reflecting the~~
390 ~~dominance of nd-WSII, which accounted for 42.9% of $\text{PM}_{2.5}$ mass (Fig. 1a). Fig. 1a~~
391 ~~also showed that variations in near surface AAE (AAE_{sfc}) were closely linked to~~
392 ~~changes in aerosol chemical composition mass fraction. Periods with elevated FMD~~
393 ~~fractions generally coincided with higher AAE_{sfc} , whereas intervals dominated by nd-~~
394 ~~WSII corresponded to lower values.~~

395 The overall distribution of AAE_{sfc} is summarized in Fig. 1b. The frequency
396 distribution further indicates that AAE_{sfc} ranged-rangs from 0.90 to 3.0; and was-occurs
397 most frequently between 1.10–1.502.0, with a mean value of 1.64 ± 0.32 . (mean
398 1.28 ± 0.39 ; Fig. 1b). A pronounced high- AAE_{sfc} tail (values above 2.0) occurs
399 episodically (Fig. 1b), suggesting intermittent enhancement of short-wavelength
400 absorption. Such elevated values likely resulted from winter heating emissions (Tian et
401 al., 2019; Yan et al., 2017) and mineral dust contributions (Fig. 1a), both known to raise
402 AAE (Liu et al., 2018).

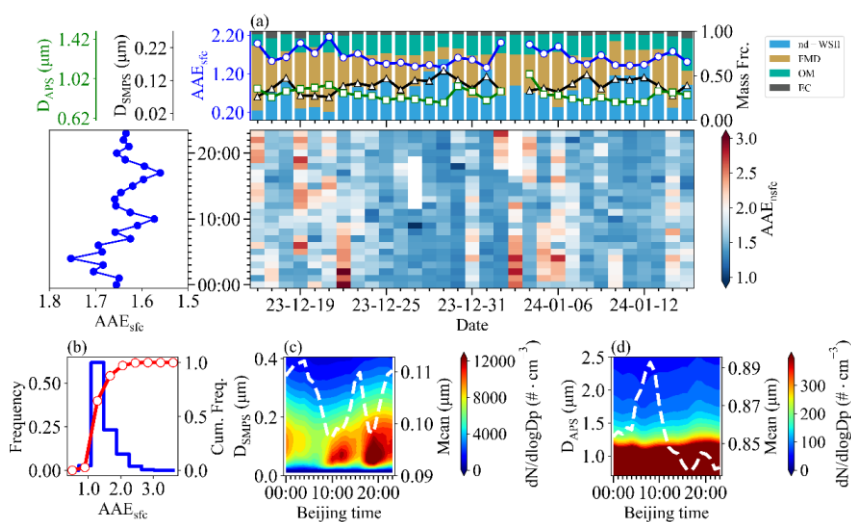
403 ~~Both absorption coefficients and AAE_{sfc} exhibited pronounced diurnal variability.~~

404 Absorption coefficients were consistently higher absorption at night and a peak around
405 23:00 (Fig. S2), driven by reduced tropospheric boundary layer height, lower afternoon
406 temperatures and wind speeds (Fig. S3), and enhanced emissions from nighttime traffic
407 and heating (Guo et al., 2016; Zhao et al., 2019).

408 The heat map in Fig. 1a further illustrates the time-of-day evolution of AAE_{sfc}
409 across the campaign, and the accompanying diurnal profile highlights a clear nighttime
410 enhancement relative to daytime. AAE_{sfc} showed a clear night-high and day-low pattern
411 (Fig. 1a), consistent with the evolution of particle size distributions. Fine-mode number
412 concentrations derived from scanning mobility particle sizer (SMPS) increased during
413 the morning rush hours and nighttime residential activity (Fig. 1c). By contrast, coarse-
414 mode diameters from aerodynamic particle sizer spectrometer (APS) were larger in the
415 early morning and decreased during the day (Fig. 1d). These results demonstrate that
416 AAE_{sfc} was co-regulated by both composition and size, providing the observational
417 evidence for the subsequent machine-learning analysis to quantify their relative
418 contributions and radiative implications.

419 Figure S6 further shows the multi-wavelength absorption coefficients and their
420 diurnal behavior. Aerosol absorption coefficients exhibit a clear spectral decrease from
421 the near-UV to the near-IR, with mean values of 13.19 ± 9.91 , 6.80 ± 6.15 , and $3.77 \pm$
422 3.27 Mm^{-1} at 375, 532, and 870 nm, respectively (mean \pm one standard deviation) (Fig.
423 S6). The corresponding mass absorption efficiencies are relatively low (0.49 ± 0.24 ,
424 0.21 ± 0.08 , and $0.12 \pm 0.04 \text{ m}^2 \cdot \text{g}^{-1}$), reflecting the dominance of nd-WSII, which

425 accounted for 42.9% of PM_{2.5} mass (Fig. 1a). Absorption coefficients at three
 426 wavelengths are consistently higher absorption at night and a peak around 23:00 (Fig.
 427 S6), driven by reduced tropospheric boundary layer height, lower afternoon
 428 temperatures and wind speeds (Fig. S7), and enhanced emissions from nighttime traffic
 429 and heating (Guo et al., 2016; Zhao et al., 2019).



430
 431 **Figure 1. Aerosol absorption characteristics during the campaign.** (a) Time series
 432 of mean particle diameters derived from SMPS and APS, mass fractions of organic
 433 matter (OM), elemental carbon (EC), non-dust water-soluble inorganic ions (nd-WSII),
 434 and fine mineral dust (FMD), together with daily averaged near-surface AAE (AAE_{sfc}).
 435 (b) Frequency distribution of AAE_{sfc} . (c–d) Diurnal variations of aerosol particle
 436 number size distributions from SMPS (c) and APS (d).

437 3.2 Influence of Composition and Size on Near-surface AAE

438 The EC mass fraction ~~showed~~ shows no correlation with AAE_{sfc} ($r = 0.09$, $p = 0.49$;

439 Fig. 2a). ~~This is plausible because EC is an operational thermal fraction and does not~~
440 ~~directly represent the optically effective BC absorption, which can be substantially~~
441 ~~modified by mixing state and coating (Petzold et al., 2013).~~ ~~which can be attributed to~~
442 ~~the weak wavelength dependence of EC absorption (Samset et al., 2018) and its~~
443 ~~relatively small mass contribution (~4%) (Fig. 2a).~~ Similarly, the OM mass fraction is
444 not significantly correlated with AAE_{sfc} ($r = -0.11$, $p = 0.40$; Fig. 2a). In contrast to
445 study dominated by biomass burning, where light-absorbing organic carbon can
446 account for > 50% of the mass fraction and strongly enhance AAE (Wang et al., 2021).
447 During the Beijing campaign, however, OM ~~contributed-contributes~~ only ~19% of total
448 $PM_{2.5}$ mass and BrC fractions ~~therefore were are~~ relatively low. Although BrC exhibits
449 intrinsically high AAE values (Laskin et al., 2015; Moosmüller et al., 2011), its impact
450 ~~was-is~~ diminished in the mixed aerosol matrix due to the influence of other dominant
451 compositions.

452 We observed a statistically significant negative correlation between AAE_{sfc} and
453 carbonaceous aerosol AAE (AAE_{CA}) (Fig. 2b), indicating that the non-carbonaceous
454 aerosol had a significantly stronger role in shaping the absorption spectral dependence
455 under complex pollution conditions. Due to nitrogen dioxide (NO_2) concentrations were
456 elevated at night (Fig. S4S8), which can interfere with PAX instruments, particularly at
457 shorter wavelengths (Arnott et al., 2000; Gyawali et al., 2012). Therefore, we restrict
458 the analysis here to daytime data (Fig S5S9). This pattern therefore cannot be ascribed
459 simply to inter-instrument discrepancies.

460 AAE_{sfc} ~~exhibited~~ exhibites a significant positive correlation with the mass fraction
461 of FMD ($r = 0.79$, $p < 0.01$) and a negative correlation with nd-WSII ($r = -0.78$, $p <$
462 0.01) (Fig. 2a). The AAE_{sfc} enhancement associated with FMD can be attributed to
463 metal oxides such as hematite and goethite, which strongly absorb in the UV
464 wavelengths and steepen the spectral dependence (Bi et al., 2016). By contrast, nd-
465 WSII (mostly sulfates, nitrates, and ammonium particles) primarily behaves as a weakly
466 absorbing (nearly scattering-only) component in the visible–near-infrared (Seinfeld &
467 Pandis, 2016), and an increase in its mass fraction therefore tends to dilute the
468 contribution of absorbing species to total PM_{2.5} absorption. In our surface dataset, this
469 dilution effect is expected to reduce the relative importance of short-wavelength
470 absorbers and, in turn, weaken the apparent wavelength dependence of bulk absorption,
471 leading to lower AAE_{sfc} when nd-WSII dominates. ~~nd-WSII acted as non-absorbing~~
472 ~~diluents, suppressing the overall wavelength dependence. We note that a “lensing effect”~~
473 ~~associated with non-absorbing coatings has been reported to enhance AAE_{CA}.~~ ~~Although~~
474 ~~the “lensing effect” of nd-WSII can enhance the AAE_{CA} (Cappa et al., 2012; Zhang et~~
475 ~~al., 2025), (Cappa et al., 2012; Zhang et al., 2025). However, the carbonaceous~~
476 ~~components contributed only a small fraction of PM_{2.5} mass during our campaign.~~
477 ~~Consequently, any potential lensing-related enhancement was likely too small relative~~
478 ~~to the total aerosol and variability to yield a detectable positive correlation between~~
479 ~~AAE_{sfc} and the nd-WSII mass fraction. In this regime, nd-WSII is better interpreted as~~
480 ~~a marker of secondary inorganic aerosol loading that mainly increases scattering and~~

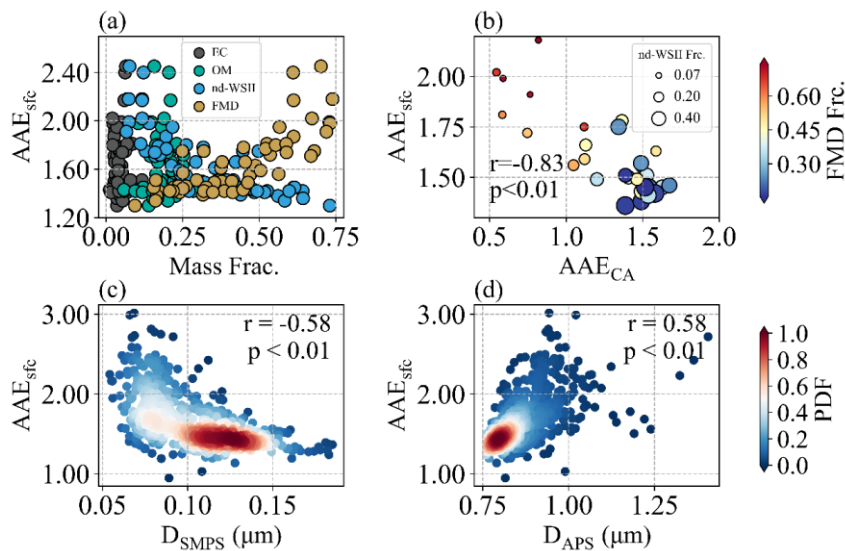
481 ~~dilutes absorber fractions due to the very low contribution of carbonaceous components~~
482 ~~to total PM_{2.5} mass, preventing any observable positive correlation between AAE_{sfc} and~~
483 ~~the nd-WSII mass fraction.~~

484 Particle size also ~~played~~ plays a critical role. AAE_{sfc} ~~was~~ is negatively associated
485 with the fine-mode mean diameter from SMPS (D_{SMPS} , $r = -0.58$; Fig. 2c) and positively
486 associated with the coarse-mode mean diameter from APS (D_{APS} , $r = 0.58$; Fig. 2d).

487 ~~Here, the correlation analysis is used as an exploratory step to describe these first-order~~
488 ~~relationships, whereas the standardized multiple linear regression (MLR) estimates the~~
489 ~~multivariate associations after accounting for predictor covariation. Consistent with the~~
490 ~~bivariate results, the MLR yields a negative standardized coefficient for D_{SMPS} (-0.02)~~
491 ~~and a positive coefficient for D_{APS} (0.44), confirming that the coarse-mode size metric~~
492 ~~provides the stronger size-related contribution in the multivariate setting.~~

493 ~~The composition terms show a similarly coherent pattern across the two analyses.~~
494 ~~FMD is positively associated with AAE_{sfc} in the bivariate correlations and remains~~
495 ~~positive in the MLR (0.35), whereas nd-WSII shows a negative association and remains~~
496 ~~negative in the MLR (-0.16). Importantly, particle size and composition are not~~
497 ~~independent in this winter dataset. Periods with larger coarse-mode diameters tend to~~
498 ~~coincide with enhanced fine mineral dust fraction ($r=0.64$; Fig. S10), consistent with~~
499 ~~stronger dust influence. Conversely, periods characterized by smaller fine-mode~~
500 ~~diameters are associated with elevated nd-WSII fraction ($r=0.89$; Fig. S10), consistent~~
501 ~~with secondary inorganic build-up and hygroscopic growth that increase scattering and~~

502 dilute the relative contribution of absorbing components. Together, these relationships
 503 results indicate that higher AAE_{sfc} is associated with a regime of larger particles and
 504 stronger dust contribution, whereas lower AAE_{sfc} occurs when secondary inorganic
 505 matter is more influential and dust contributions are reduced. larger particles coincide
 506 with higher FMD and lower nd-WSII, enhancing AAE_{sfc} , whereas smaller particles
 507 favor inorganic salts and reduced dust contributions, lowering AAE_{sfc} . Overall, AAE_{sfc}
 508 is influenced not only by carbonaceous aerosols, but also strongly by other chemical
 509 components, particularly mineral dust-related particles, non-dust water-soluble
 510 inorganic ions, and particle-size distributions. was not governed by carbonaceous
 511 aerosols alone but rather by the coupled influence of mineral dust, inorganic matter,
 512 and particle size distributions.

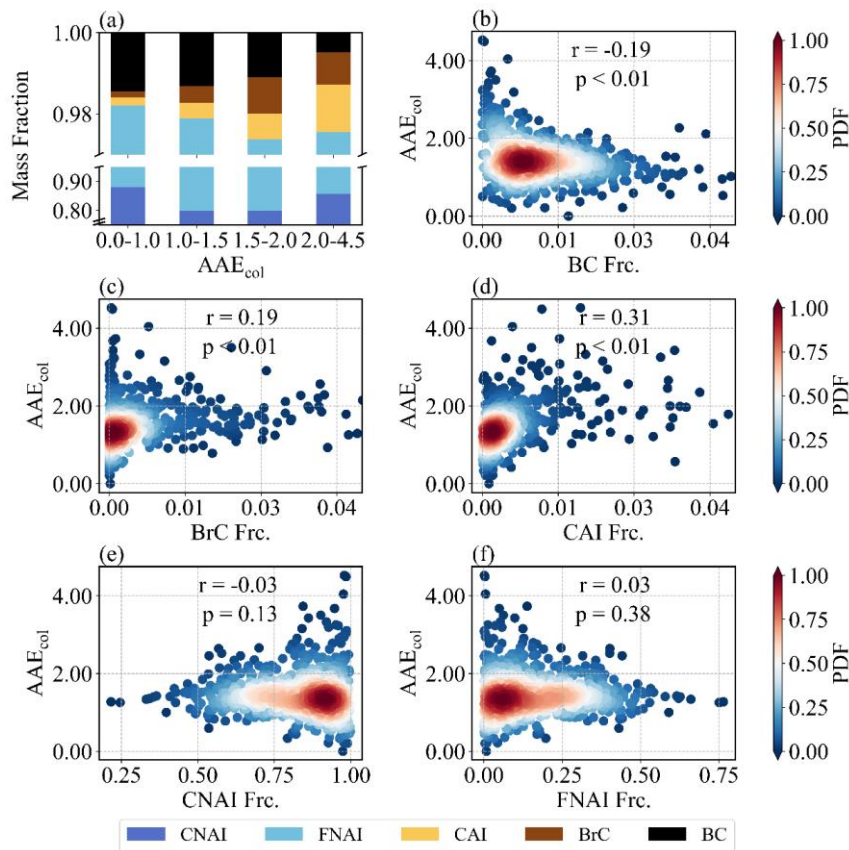


513
 514 **Figure 2. Relationships of near-surface absorption Ångström exponent (AAE_{sfc})**
 515 **with chemical composition and particle size.** (a) Scatter plots of chemical mass

516 concentration fraction and total aerosol AAE_{sfc} . (b) Relationship between AAE_{sfc} and
517 carbonaceous aerosol AAE (AAE_{CA}), with symbol size representing the non-dust
518 water-soluble ions (nd-WSII) fraction and color denoting the fine mineral dust (FMD)
519 fraction. (c–d) Correlations of AAE_{sfc} with mean particle diameters derived from SMPS
520 (c) and APS (d), respectively. Shaded colors indicate probability density.

521 3.3 Quantitative Contributions of Composition and Size to Columnar AAE

522 The relationships between mass fractions of chemical composition and AAE_{col}
523 were studied using AERONET data (Fig. 3). ~~The AAE_{col} (1.47 ± 0.56) was also~~
524 ~~suggested to be greater than that derived from the surface field campaign (Fig. 1),~~
525 ~~partially due to the vertical variation in aerosol absorption (Guan et al., 2024).~~ The
526 CNAI and FNAI mass fractions varied little and exhibited no significant correlations
527 with AAE_{col} ($r = -0.03$ and 0.03 , $p > 0.1$), indicating a negligible role in setting the
528 absorption spectral dependence. In contrast, BC, BrC, and CAI displayed clear
529 associations. Higher AAE_{col} (>1.5) were associated with marked increases in BrC and
530 CAI, whereas lower AAE_{col} (<1.5) corresponded to relatively higher BC contributions.
531 Correlation analysis is consistent with these patterns: AAE_{col} was negatively correlated
532 with BC ($r = -0.19$, $p < 0.01$), in line with its weak wavelength dependence, but
533 positively correlated with BrC ($r = 0.19$, $p < 0.01$) and CAI ($r = 0.31$, $p < 0.01$),
534 underscoring the strong wavelength dependence of BrC and dust. These findings were
535 similarly to our surface campaign, particularly regarding dust's amplifying effect on
536 AAE_{col} .



537

538 **Figure 3. Relationships between columnar absorption Ångström exponent (AAE_{col})**

539 **and major aerosol chemical compositions.** (a) Mass fractions of fine-mode non-

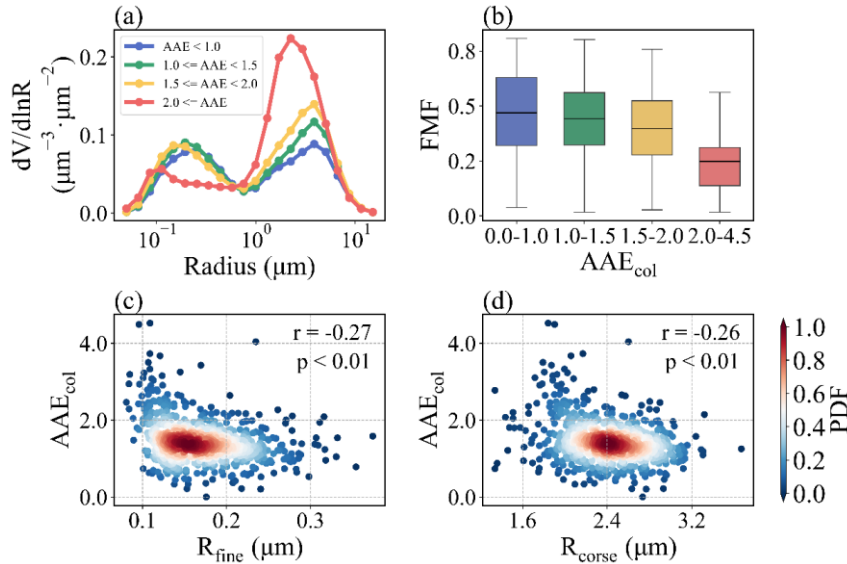
540 absorbing soluble matter (FNAI), coarse-mode non-absorbing soluble matter (CNAI),

541 coarse-mode absorbing soluble matter (CAI, representing dust), brown carbon (BrC),

542 and black carbon (BC) across different AAE_{col} bins. (b-f) Correlations between AAE_{col}

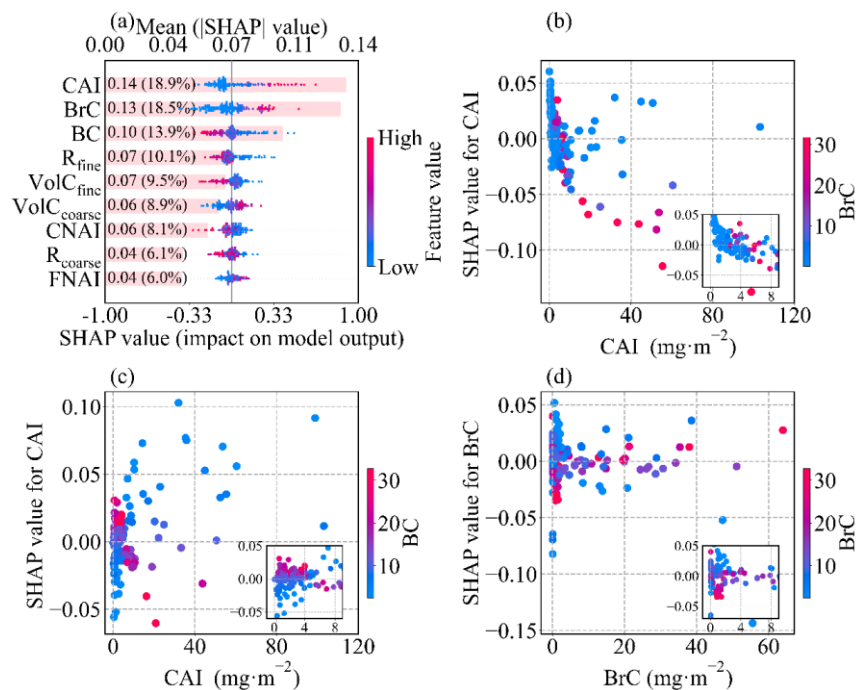
543 and the mass fractions of BC, BrC, CAI, CNAI, and FNAI, respectively; shaded colors

544 denote probability density.



545
 546 **Figure 4. Relationships between columnar absorption Ångström exponent (AAE**
 547 **col) and aerosol size distribution characteristics.** (a) Volume size distributions
 548 grouped by AAE_{col} bins. (b) Fine-mode fraction (FMF) by AAE_{col} bins, with horizontal
 549 lines indicating means. (c–d) Correlations of AAE_{col} with effective radius of fine-mode
 550 (R_{fine}) and coarse-mode (R_{coarse}) particles, respectively.

551 The impacts of aerosol size distribution on AAE_{col} were clearly reflected (Fig. 4).
 552 With AAE_{col} increasing, the peaks of both fine and coarse modes shifted to smaller sizes
 553 (Fig. 4a), indicating an overall refinement of the size distribution. The R_{fine} and R_{coarse}
 554 were both negatively correlated with AAE_{col} (r = -0.27 and -0.26, p < 0.01; Fig. 4c,
 555 4d), demonstrating that reductions in particle size in both modes enhanced the spectral
 556 dependence. Interestingly, FMF decreased with increasing AAE_{col} (Fig. 4b), suggesting
 557 that coarse-mode particles retained a substantial volumetric contribution even under
 558 high AAE_{col} conditions.



559

560 **Figure 5. SHAP interpretation of the machine-learning model for columnar AAE.**

561 (a) Attribution of chemical compositions and particle size parameters to columnar AAE.

562 Each horizontal bar represents the mean absolute SHAP value of a feature, indicating

563 its overall impact on the model output; the color gradient shows the effect of feature

564 values on columnar AAE, with red indicating a positive influence and blue indicating a

565 negative influence. Features are ranked by importance. (b-c) SHAP dependence plots

566 corresponding to CAI. (d) SHAP dependence plots corresponding to BrC.

567 Machine learning analysis further quantified relative contributions, as illustrated

568 in Fig. 5a. It is found that showed that CAI had the strongest explanatory power,

569 accounting for ~19% of the model's predictive power~~model performance~~, confirming

570 the dominant role of dust in amplifying spectral absorption. BrC was second (18.5%)

571 and BC was third (13.9%), together with CAI explaining ~50% of model's predictive
572 power (as measured by mean absolute SHAP value) model performance. Among the
573 size-related predictors, R_{fine} alone accounted for about one quarter (~29%) of the
574 cumulative importance of all size metrics, making it the most influential size parameter.

575 In addition, ~~its~~ its importance was also clearly higher than CNAI and FNAI (Fig. 5a),
576 indicating that the mean radius of fine mode particles is the key size control on AAE_{col} .

577 During the prediction process, it is observed that higher values of BrC, CAI, and volume
578 concentrations of coarse-mode ($\text{vol}_{\text{coarse}}$) corresponded to higher SHAP values and
579 higher values of other predictors corresponded to smaller SHAP values (Fig. 5a). These
580 responses are fully consistent with the correlations between AAE_{col} and these
581 parameters (Fig. 3b–d; Fig. 4c–d). Collectively, these results demonstrated that AAE_{col}
582 is not governed by BC or BrC alone; it is primarily modulated by dust and secondarily
583 by particle size structure (size metrics together ~35%), underscoring the need to
584 account for both composition and size when evaluating spectral absorption.

585 To connect these statistical attributions to physically plausible behavior, we
586 performed a simple Mie-theory sensitivity analysis (Text S3; Fig. S11). First, we varied
587 the imaginary part of the refractive index at 440 nm (k_{440}) while keeping the size
588 distribution fixed. Second, keeping refractive index fixed and shifting the fine- and
589 coarse-mode radii to 80%, 90%, 100%, 110%, and 120% of their baseline values (with
590 mode-integrated volume conserved).

591 Varying k_{440} produces a substantially larger change in the modeled AAE_{col} than the

592 size-shift experiments (Fig. S12), indicating that changes in short-wavelength
593 absorptivity exert stronger leverage on AAE than variations in modal radii. Because we
594 altered k_{440} while keeping k_{870} unchanged, this experiment specifically isolates
595 enhanced absorption in the short wavelengths which is consistent with increased
596 contributions from aerosols that preferentially absorb at shorter wavelengths, such as
597 absorbing mineral dust and brown carbon. Spectral refractive indices retrieved by
598 AERONET are known to vary systematically across aerosol types and can be used to
599 infer absorbing components, supporting the interpretation of k as a proxy for
600 composition-related absorption variability (Dubovik et al., 2002; Wang et al., 2013).
601 Fine-mode shifts produce a clearer change in the AAE_{col} than coarse-mode shifts (Fig.
602 S12b, S12c), consistent with R_{fine} being the leading size predictor in Fig. 5a. Taken
603 together, the SHAP results and the Mie sensitivity tests support a consistent
604 interpretation that AAE_{col} is not influenced by BC or BrC alone; it is primarily
605 associated with dust and secondarily by particle-size structure (size metrics together
606 ~35%) (Fig. 5a), underscoring the need to account for both composition and size when
607 evaluating spectral absorption.

608 To further investigate the interaction effects of major parameters on AAE_{col}
609 prediction, we selected CAI, BrC, and BC, the three most influential predictors by
610 SHAP, to analyze their interactions (Fig. 5b-5f). When CAI loading was below 10
611 $\text{mg}\cdot\text{m}^{-2}$, BrC suppressed the positive impact of CAI loading and progressively drove it
612 toward a negative contribution. When CAI loading exceeded $10\text{ mg}\cdot\text{m}^{-2}$, lower BrC is

613 more likely than higher BrC to sustain or enhance the positive marginal effect of CAI,
614 although the magnitude is weaker than in the CAI loading $< 10 \text{ mg}\cdot\text{m}^{-2}$ regime. For
615 CAI loading in the range 0–4, higher BC yielded a positive marginal effect of CAI on
616 AAE_{col} , whereas lowed BC yielded a negative one. Once CAI loading is greater than 4
617 $\text{mg}\cdot\text{m}^{-2}$, this relationship reverses, with higher BC more likely to make further increases
618 in CAI contribute negatively to AAE_{col} . As BrC increases, BC progressively reduces
619 the positive and negative contributions of BrC to AAE_{col} . These interactions indicate
620 that models of aerosol spectral absorption should explicitly represent the mutual
621 constraints among CAI, BrC, and BC to better identify and quantify AAE drivers.

622 **3.4 The comparison between surface and columnar AAE.**

623 Sections 3.2 and 3.3 provide two complementary perspectives on AAE. The near-
624 surface campaign (December 2023–January 2024) represents a specific winter
625 pollution regime, whereas the AERONET analysis provides a longer-term perspective
626 (2001–2019). Despite these differences, the two analyses converge on a consistent
627 mechanistic interpretation. AAE increases when short-wavelength absorption becomes
628 relatively stronger, and dust-related absorption plays a central role in influencing this
629 spectral dependence. In the surface analysis, the fine mineral dust fraction within $\text{PM}_{2.5}$
630 is significantly associated with elevated AAE_{sf} (Fig. 2a). In the column analysis, the
631 absorbing dust component (CAI), which includes substantial coarse-mode
632 contributions (radius about 0.6–15 μm), likewise ranks among the most informative
633 predictors for AAE_{col} (Fig. 5a). Despite the different size ranges and vertical weighting,

634 both indicators consistently support the interpretation that dust-related enhancement of
635 short-wavelength absorption, and is linked to higher AAE.

636 It is also worth noting that the AAE_{col} (1.47 ± 0.56) was found to be lower than
637 that derived from the surface field campaign (Fig. 1), but this difference should not be
638 interpreted as a comparison between column and surface values. The two quantities
639 differ in both temporal representativeness (multi-year climatology versus a one-month
640 winter campaign) and measurement definition (AAOD-based column integration
641 versus near-surface absorption coefficients), so their absolute magnitudes are expected
642 to vary with aerosol regime, meteorology, and the contribution of elevated layers.
643 Therefore, our emphasis is on the consistency of predicting factors and mechanisms,
644 rather than a direct comparison of mean values.

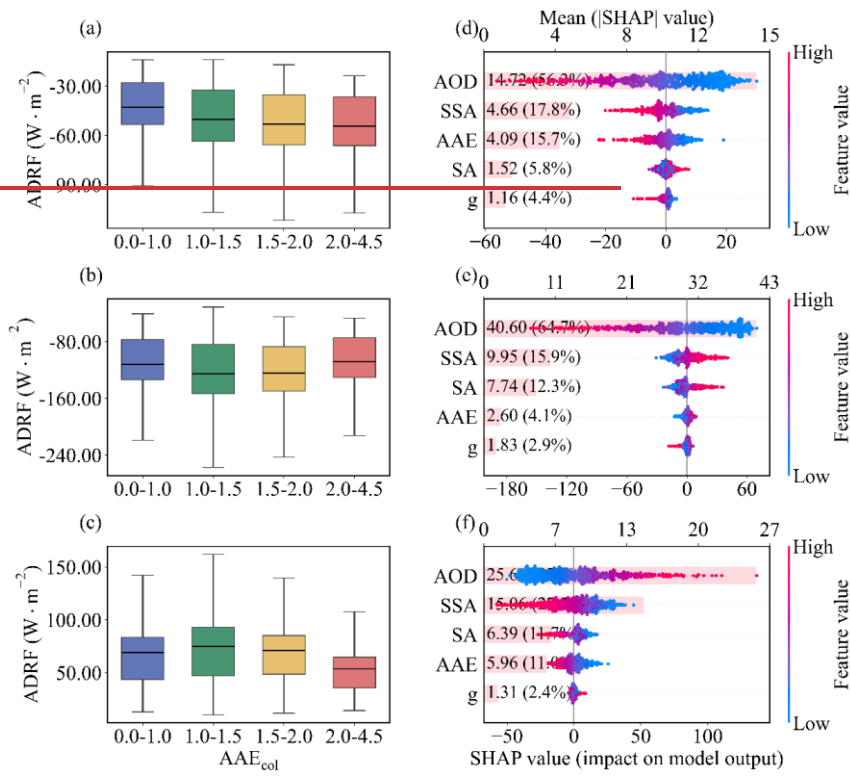
645 Finally, the two datasets complement each other in terms of strengths and
646 limitations. The surface measurements provide chemically explicit constraints but are
647 restricted to $PM_{2.5}$, thereby under-representing coarse-mode dust and any elevated-layer
648 contributions. The AERONET analysis offers direct links to radiative quantities, but its
649 component variables are retrieval-based optical constructs that depend on prescribed
650 optics and mixing assumptions (Dubovik et al., 2000; Sinyuk et al., 2020; Li et al.,
651 2019). As a result, several categories are not directly interchangeable (e.g., surface nd-
652 WSII versus retrieved non-absorbing components, surface OM versus optically defined
653 BrC, and thermal EC versus optically defined BC). Taken together, the surface
654 campaign provides process-level chemical context for short-term variability, while the

655 AERONET record generalizes the interpretation across regimes and links AAE to
656 column radiative effects with dust-related absorption emerging as the clearest cross-
657 scale consistency.

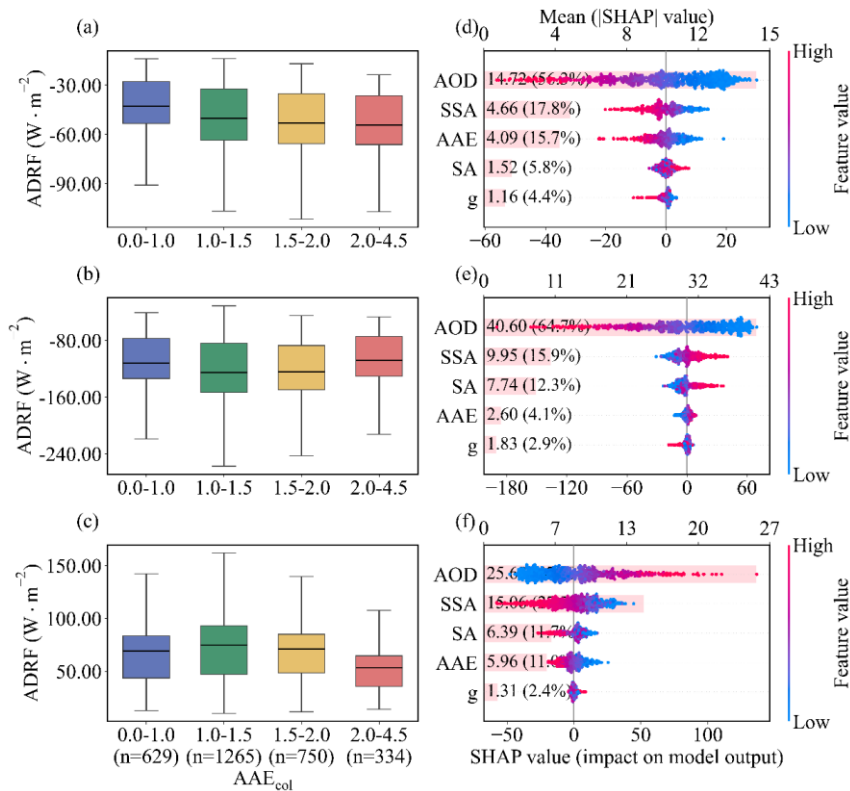
658 **3.4–5 The Diagnostic Power of Columnar AAE for Radiative Forcing and** 659 **Efficiency Responses to Columnar AAE in Beijing**

660 Joint analysis of the boxplots and SHAP diagnostics revealed a robust, layer-
661 dependent correlationcoupling between the AAE_{col} and ADRF. As AAE_{col} increased
662 increases from 0–1 to 2–4.5, cooling at the TOA intensifies, atmospheric heating
663 weakenedweakens, and cooling at the BOA was is alleviated (Fig. 6a-6c-). This pattern
664 is consistent with a shift from more BC-like absorption toward regimes with stronger
665 short-wavelength absorption signatures and higher scattering fractions, commonly
666 associated with mixtures involving BrC and mineral dust, reflecting a transition from
667 BC-dominated, low SSA conditions to high SSA regimes influenced by BrC and
668 mineral dust. SHAP method confirmed that AAE_{col} is the third strongest predictordriver
669 (~16%) after AOD (~56%), and comparably to SSA (~18%) at TOA and consistently
670 shifts ADRF toward more negative values (Fig. 6d). At BOA, AAE_{col}
671 explaincontributes only ~4% of the model importance. BOA cooling is primarily
672 explainedregulated by AOD (~65.0%) and SSA (~16 %) (Fig. 6e). In the ATM, AOD
673 and SSA remain the leading predictors, whilejointly dominated, but AAE_{col} still shows
674 importance comparablecontributed comparably to surface albedo (SA) (both ~12%)
675 (Fig. 6f), underscoring its role in vertically redistributing radiative energy.

676 Mechanistically, higher AAE_{col} is commonly associated with BrC and dust, which
 677 exhibit higher SSA but lower mass absorption efficiencies (MAE), thereby enhancing
 678 backscattering and solar escape (more negative TOA forcing), reducing absorption
 679 (weaker atmospheric heating), and producing a net transmission effect that mitigates
 680 BOA cooling.



681



682

683 **Figure 6.** The relationship between columnar AAE (AAE_{col}) and aerosol direct

684 radiative forcing (ADRF). Role of columnar absorption Ångström exponent (AAE_{col})

685 in regulating aerosol direct radiative forcing (ADRF). (a–c) Box plots of ADRF at

686 the top of the atmosphere (a), bottom (b), and in the atmosphere (c) as a function of

687 AAE_{col} . The sample sizes for the AAE_{col} bins 0.0–1.0, 1.0–1.5, 1.5–2.0, and 2.0–4.5 are

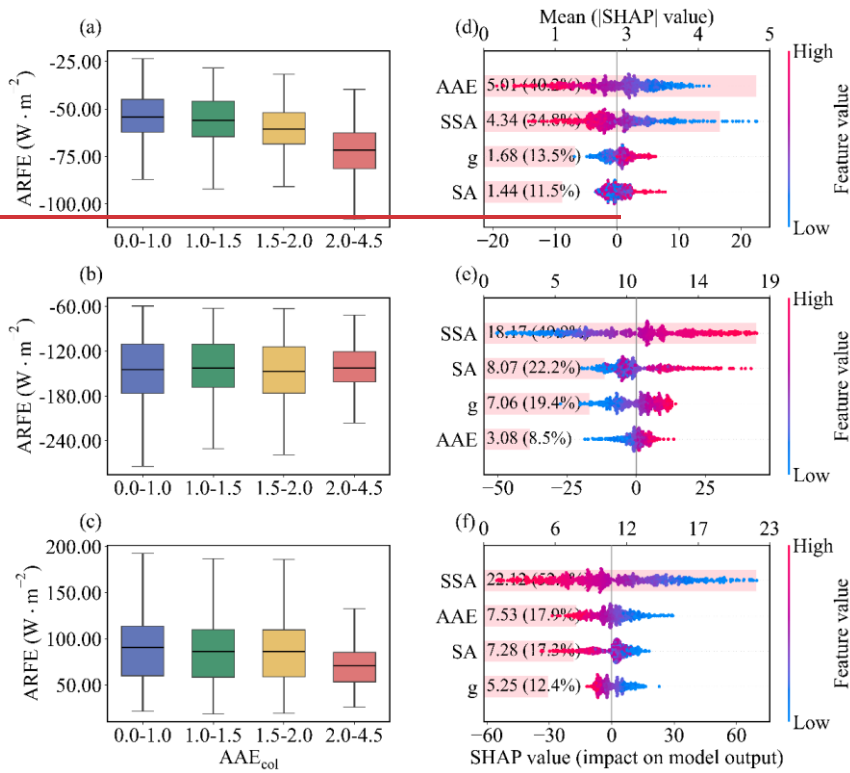
688 $n = 629, 1265, 750,$ and $334,$ respectively, and are identical for panels (a)–(c). (d–f)

689 SHAP analysis quantifies the relative contributions of aerosol optical depth (AOD),

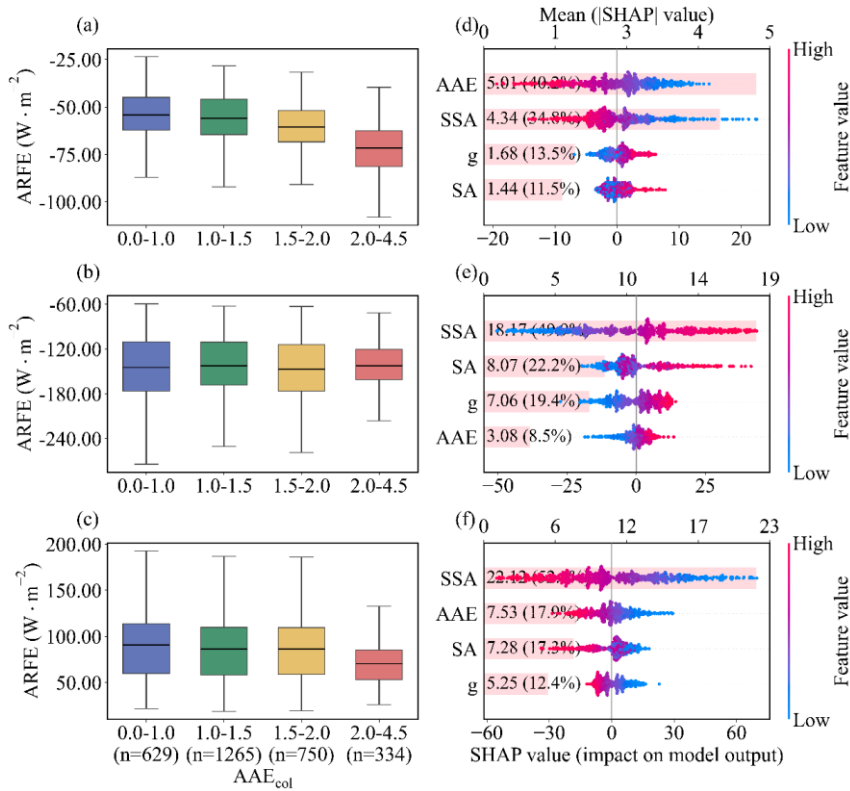
690 single scattering albedo (SSA), asymmetry parameter (g), surface albedo (SA) and

691 AAE_{col} in driving-predicting ADRF variations at the top of the atmosphere (d), at the

692 bottom of the atmosphere (e), and in the atmosphere (f). The mean absolute SHAP
 693 values (numbers in parentheses) indicate the relative contribution of each predictor to
 694 the model output.



695



696
 697 **Figure 7.** The relationship between columnar AAE (AAE_{col}) and aerosol radiative
 698 forcing efficiency (ARFE). Role of columnar absorption Ångström exponent
 699 (AAE_{col}) in regulating aerosol radiative forcing efficiency (ARFE). (a–c) Box plots
 700 of ARFE at the top of the atmosphere (a), bottom (b), and in the atmosphere (c) as a
 701 function of AAE_{col}. The sample sizes for the AAE_{col} bins 0.0–1.0, 1.0–1.5, 1.5–2.0, and
 702 2.0–4.5 are n = 629, 1265, 750, and 334, respectively, and are identical for panels (a)–
 703 (c). (d–f) SHAP analysis with AOD fixed at its median (50th percentile) quantifies the
 704 relative contributions of single scattering albedo (SSA), asymmetry parameter (g),
 705 surface albedo (SA) and AAE_{col} in driving-predicting ARFE variations at the top of the

706 atmosphere (d), bottom (e), and in the atmosphere (f). The mean absolute SHAP values
707 (numbers in parentheses) indicate the relative contribution of each predictor to the
708 model output.

709 To better show columnar AAE's impact on ADRF, we introduced the ARFE,
710 which removes the scaling by aerosol loading and highlights intrinsic optical controls.
711 At TOA, AAE_{col} ~~is~~ serves as a key diagnostic of ~~was the dominant driver of~~ cooling
712 efficiency in the model, based on ~~with~~ mean $|SHAP|$ reaching ($\sim 40.0\%$), exceeding the
713 asymmetry factor (g), SSA, and SA even when AOD was conditioned at 25th (Fig.
714 ~~S10S12~~), 50th (Fig. 7), 75th percentiles (Fig. ~~S11S13~~), or mean (Fig. ~~S12S14~~). Larger
715 AAE_{col} ~~was~~ is associated with more negative TOA ARFE (Fig. 7d), indicating that, for
716 comparable loading, regimes with steeper absorption spectra tend to exhibit stronger
717 TOA cooling efficiency, consistent with stronger shortwave backscattering by BrC and
718 dust (Fig. 7d). At BOA, ARFE ~~was~~ is ~~predicted~~ governed primarily by SSA ($\sim 50\%$),
719 followed by g and SA, with AAE_{col} ~~contributing~~ predicting more modestly ($\sim 8\%$, %) (
720 Fig. 7e). In this layer, higher SSA and larger g tend to make ARFE less negative,
721 consistent with reduced absorption and more forward-directed scattering leading to
722 greater transmittance for a fixed AOD. ~~increases in SSA and g tended to make ARFE~~
723 ~~less negative (Fig. 7e), indicative of enhanced forward scattering and greater~~
724 ~~transmittance for a fixed AOD.~~ In the ATM, SSA is the dominant predictor of ~~dominated~~
725 the heating-efficiency ($>50\%$), with AAE_{col} and SSA-SA providing secondary ~~control~~
726 information (both $\sim 17\%$), while g played a minor role (Fig. 7f). Higher AAE_{col} is linked

727 to lower atmospheric heating efficiency, reflecting a shift toward aerosol types with
728 weaker mass absorption than BC, and higher SSA further suppresses in-column
729 absorption. Overall, these results do not imply that AAE_{col} is a causal driver of radiative
730 forcing and radiative forcing efficiency; rather, AAE_{col} acts as a compact descriptor of
731 absorption spectral shape that co-varies with underlying composition and size regimes.
732 The strong association between radiative forcing and ARFE therefore suggests that
733 constraining AAE can meaningfully improve estimates of forcing efficiency in
734 radiative assessments.

735 **4 Conclusions**

736 LAAs exert a strong influence on the Earth's radiation budget, yet the spectral
737 dependence of their absorption, commonly summarized by the AAE, remains poorly
738 constrained in urban regions. Here we combined a winter in situ observation in Beijing
739 with a long-term AERONET column data (2001–2019) and an interpretable machine-
740 learning framework to quantify how composition and particle size influence AAE and
741 to evaluate what AAE implies for radiative effects, disentangle the drivers of the AAE
742 and to clarify its radiative implications.

743 Near the surface in wintertime Beijing, AAE variability co-varied primarily with
744 enhanced fractions of fine mineral dust and water-soluble inorganic ions, underscoring
745 that non-carbonaceous species can substantially modulate local absorption spectra in
746 addition to BC and BrC. At the column level, SHAP diagnostics identified CAI is the

747 ~~most informative as the leading driver predictor~~ of columnar AAE, followed by BrC and
748 BC. Among particle size metrics, the fine-mode effective radius is the leading size-
749 related predictor~~emerged as the most influential variable~~ and ~~accounted~~accounts for
750 about 29% of the cumulative importance of all size parameters, whereas non-absorbing
751 composition (coarse and fine non-absorbing dust and non-absorbing carbonaceous
752 aerosols) played only a minor role. Because this study is based on Beijing observations,
753 the identified predictor importance reflects a polluted urban environment influenced by
754 both anthropogenic aerosol and episodic dust. In cleaner regions the relationships may
755 weaken due to lower absorption signal, whereas in more dust- influenced regions the
756 role of dust-related predictors would likely become even stronger.

757 For radiative impacts, our results highlight the diagnostic value of columnar AAE
758 rather than implying a causal control. In the model trained on AERONET radiative
759 products, The radiative analysis shows that columnar AAE is a key regulator of ADRF
760 at the TOA. Columnar AAE is among the most informative predictors for
761 TOA ADRF (~16%, comparable to SSA) explained about 16% of the variance in TOA
762 ADRF, comparable to the contribution from SSA, and ~~became~~ becomes the leading
763 predictor ~~of~~ for TOA ARFE (~40%), with higher columnar AAE associated with more
764 efficient TOA cooling under loading-controlled conditions, accounting for roughly 40%
765 of its variability and systematically enhancing TOA cooling efficiency. By contrast,
766 columnar AAE contributes much less to the prediction of ATM and BOA ADRF and
767 ARFE, where AOD and SSA remain the primary predictors, the direct influence of AAE

768 ~~on ADRF and ARFE in the ATM and at the BOA was clearly weaker, where SSA and~~
769 ~~loading-related quantities remained dominant.~~

770 Overall, The—the findings of our study demonstrate the multifactorial
771 influencecontrol of AAE by composition and size and highlight its strong correlation
772 with the vertical partitioning of radiative forcing, highlight its pivotal role in partitioning
773 radiative forcing vertically among TOA, ATM, and BOA, especially at the TOA.
774 Consequently, accurately constraining AAE ~~and its drivers~~ is essential for a realistic
775 representation of aerosol radiation interactions in regional and global models.

776 **Data and code availability**

777 The data that support the findings of this study are available in the Zenodo data
778 repository (<https://doi.org/10.5281/zenodo.17852818>, Wang et al., 2025b). The
779 AERONET data is freely available on the AERONET website
780 (<https://aeronet.gsfc.nasa.gov/>). The aerosol chemical composition derived from
781 AERONET inversion data is available from [https://doi.org/10.1175/BAMS-D-23-](https://doi.org/10.1175/BAMS-D-23-0260.1)
782 [0260.1](https://doi.org/10.1175/BAMS-D-23-0260.1). The code scripts are also available in the Zenodo data repository
783 (<https://doi.org/10.5281/zenodo.17852818>, Wang et al., 2025b).

784 **Acknowledgments**

785 We thank the AERONET PI at the Beijing site for their efforts in establishing and
786 maintaining the site. We are also grateful to Prof. Yunfei Wu for providing access to the

787 experimental facilities at the Institute of Atmospheric Physics, Chinese Academy of
788 Sciences. We also thank the Lanzhou University Supercomputing Center for providing
789 computational support.

790 **Financial supports**

791 This research was supported by the National Natural Science Foundation of China
792 (42475080), the Gansu Province Graduate Innovation Funding Project (2025CXZX-
793 177) and the Fundamental Research Funds for the Central Universities (lzujbky-2024-
794 ey04).

795 **Author contribution**

796 PT designed the study. PT and WW received the funding. WW, PT, SZ, ZY and
797 MC analyzed the data and led the writing. WW, YZ, YW and PT conducted the field
798 campaign. WW, PT, SZ, YZ, ZY, CC, YW, MC and LZ contributed to discussion, review,
799 and edit the manuscript.

800 **Competing interests**

801 The authors declare that they have no conflict of interest.

802 **References**

- 803 Ångström, A.: On the Atmospheric Transmission of Sun Radiation and on Dust in the
804 Air, *Geografiska Annaler*, 11, 156–166,
805 <https://doi.org/10.1080/20014422.1929.11880498>, 1929.
- 806 Arnott, W. P., Moosmüller, H., and Walker, J. W.: Nitrogen dioxide and kerosene-flame
807 soot calibration of photoacoustic instruments for measurement of light absorption
808 by aerosols, *Review of Scientific Instruments*, 71, 4545–4552,
809 <https://doi.org/10.1063/1.1322585>, 2000.
- 810 Bahadur, R., Praveen, P. S., Xu, Y., and Ramanathan, V.: Solar absorption by elemental
811 and brown carbon determined from spectral observations, *Proc. Natl. Acad. Sci.*
812 *U.S.A.*, 109, 17366–17371, <https://doi.org/10.1073/pnas.1205910109>, 2012.
- 813 [Bergstrom, R. W., Pilewskie, P., Russell, P. B., Redemann, J., Bond, T. C., Quinn, P. K.,](#)
814 [and Sierau, B.: Spectral absorption properties of atmospheric aerosols, *Atmos.*](#)
815 [*Chem. Phys.*, 7, 5937–5943, <https://doi.org/10.5194/acp-7-5937-2007>, 2007.](#)
- 816 Bi, J., Huang, J., Holben, B., and Zhang, G.: Comparison of key absorption and optical
817 properties between pure and transported anthropogenic dust over East and Central
818 Asia, *Atmos. Chem. Phys.*, 16, 15501–15516, [https://doi.org/10.5194/acp-16-](https://doi.org/10.5194/acp-16-15501-2016)
819 [15501-2016](#), 2016.
- 820 Cappa, C., Kotamarthi, R., Selacek, A., Flynn, C., Lewis, E., McComiskey, A., and
821 Riemer, N.: Absorbing Aerosols Workshop Report, January 20–21, 2016,

822 <https://doi.org/10.2172/1471231>, 2016.

823 Cappa, C. D., Onasch, T. B., Massoli, P., Worsnop, D. R., Bates, T. S., Cross, E. S.,
824 Davidovits, P., Hakala, J., Hayden, K. L., Jobson, B. T., Kolesar, K. R., Lack, D.
825 A., Lerner, B. M., Li, S.-M., Mellon, D., Nuaaman, I., Olfert, J. S., Petäjä, T.,
826 Quinn, P. K., Song, C., Subramanian, R., Williams, E. J., and Zaveri, R. A.:
827 Radiative Absorption Enhancements Due to the Mixing State of Atmospheric
828 Black Carbon, *Science*, 337, 1078–1081, <https://doi.org/10.1126/science.1223447>,
829 2012.

830 Cazorla, A., Bahadur, R., Suski, K. J., Cahill, J. F., Chand, D., Schmid, B., Ramanathan,
831 V., and Prather, K. A.: Relating aerosol absorption due to soot, organic carbon, and
832 dust to emission sources determined from in-situ chemical measurements, *Atmos.*
833 *Chem. Phys.*, 13, 9337–9350, <https://doi.org/10.5194/acp-13-9337-2013>, 2013.

834 Chakrabarty, R. K., Arnold, I. J., Francisco, D. M., Hatchett, B., Hosseinpour, F., Loria,
835 M., Pokharel, A., and Woody, B. M.: Black and brown carbon fractal aggregates
836 from combustion of two fuels widely used in Asian rituals, *Journal of Quantitative*
837 *Spectroscopy and Radiative Transfer*, 122, 25–30,
838 <https://doi.org/10.1016/j.jqsrt.2012.12.011>, 2013.

839 Chow, J. C., Watson, J. G., Chen, L.-W. A., Chang, M. C. O., Robinson, N. F., Trimble,
840 D., and Kohl, S.: The IMPROVE_A Temperature Protocol for Thermal/Optical
841 Carbon Analysis: Maintaining Consistency with a Long-Term Database, *Journal*
842 *of the Air & Waste Management Association*, 57, 1014–1023,

843 <https://doi.org/10.3155/1047-3289.57.9.1014>, 2007.

844 Cuesta-Mosquera, A., Glojek, K., Močnik, G., Drinovec, L., Gregorič, A., Rigler, M.,
845 Ogrin, M., Romshoo, B., Weinhold, K., Merkel, M., Van Pinxteren, D., Herrmann,
846 H., Wiedensohler, A., Pöhlker, M., and Müller, T.: Optical properties and simple
847 forcing efficiency of the organic aerosols and black carbon emitted by residential
848 wood burning in rural central Europe, *Atmos. Chem. Phys.*, 24, 2583–2605,
849 <https://doi.org/10.5194/acp-24-2583-2024>, 2024.

850 [Dubovik, O., Holben, B., Eck, T. F., Smirnov, A., Kaufman, Y. J., King, M. D., Tanré,](#)
851 [D., and Slutsker, I.: Variability of Absorption and Optical Properties of Key](#)
852 [Aerosol Types Observed in Worldwide Locations, *J. Atmos. Sci.*, 59, 590–608,](#)
853 [https://doi.org/10.1175/1520-0469\(2002\)059<0590:VOAAOP>2.0.CO;2](https://doi.org/10.1175/1520-0469(2002)059<0590:VOAAOP>2.0.CO;2), 2002.

854 [Dubovik, O. and King, M. D.: A flexible inversion algorithm for retrieval of aerosol](#)
855 [optical properties from Sun and sky radiance measurements, *J. Geophys. Res.*, 105,](#)
856 [20673–20696, <https://doi.org/10.1029/2000JD900282>, 2000.](#)

857 [Dubovik, O., Sinyuk, A., Lapyonok, T., Holben, B. N., Mishchenko, M., Yang, P., Eck,](#)
858 [T. F., Volten, H., Muñoz, O., Veihelmann, B., Van Der Zande, W. J., Leon, J.,](#)
859 [Sorokin, M., and Slutsker, I.: Application of spheroid models to account for](#)
860 [aerosol particle nonsphericity in remote sensing of desert dust, *J. Geophys. Res.*,](#)
861 [111, 2005JD006619, <https://doi.org/10.1029/2005JD006619>, 2006.](#)

862 [García, O. E., Díaz, A. M., Expósito, F. J., Díaz, J. P., Dubovik, O., Dubuisson, P., Roger,](#)
863 [J. -C., Eck, T. F., Sinyuk, A., Derimian, Y., Dutton, E. G., Schafer, J. S., Holben,](#)

864 [B. N., and García, C. A.: Validation of AERONET estimates of atmospheric solar](#)
865 [fluxes and aerosol radiative forcing by ground-based broadband measurements, J.](#)
866 [Geophys. Res., 113, 2008JD010211, <https://doi.org/10.1029/2008JD010211>, 2008.](#)

867 Gliß, J., Mortier, A., Schulz, M., Andrews, E., Balkanski, Y., Bauer, S. E., Benedictow,
868 A. M. K., Bian, H., Checa-Garcia, R., Chin, M., Ginoux, P., Griesfeller, J. J.,
869 Heckel, A., Kipling, Z., Kirkevåg, A., Kokkola, H., Laj, P., Le Sager, P., Lund, M.
870 T., Lund Myhre, C., Matsui, H., Myhre, G., Neubauer, D., Van Noije, T., North, P.,
871 Olivie, D. J. L., Rémy, S., Sogacheva, L., Takemura, T., Tsigaridis, K., and Tsyro,
872 S. G.: AeroCom phase III multi-model evaluation of the aerosol life cycle and
873 optical properties using ground- and space-based remote sensing as well as surface
874 in situ observations, *Atmos. Chem. Phys.*, 21, 87–128,
875 <https://doi.org/10.5194/acp-21-87-2021>, 2021.

876 ~~Guan, X., Tian, P., Wang, W., Zhang, M., Song, X., Zhang, Z., and Zhang, L.: More~~
877 ~~Accurate Quantification of Direct Aerosol Radiative Effects Using Vertical~~
878 ~~Profiles of Single Scattering Albedo Derived From Tethered Balloon Observations,~~
879 ~~JGR Atmospheres, 129, e2023JD040605, <https://doi.org/10.1029/2023JD040605>,~~
880 ~~2024.~~

881 Guinot, B., Cachier, H., and Oikonomou, K.: Geochemical perspectives from a new
882 aerosol chemical mass closure, *Atmos. Chem. Phys.*, 7, 1657–1670,
883 <https://doi.org/10.5194/acp-7-1657-2007>, 2007.

884 Guo, J., Miao, Y., Zhang, Y., Liu, H., Li, Z., Zhang, W., He, J., Lou, M., Yan, Y., Bian,

885 L., and Zhai, P.: The climatology of planetary boundary layer height in China
886 derived from radiosonde and reanalysis data, *Atmos. Chem. Phys.*, 16, 13309–
887 13319, <https://doi.org/10.5194/acp-16-13309-2016>, 2016.

888 Gyawali, M., Arnott, W. P., Zaveri, R. A., Song, C., Moosmüller, H., Liu, L.,
889 Mishchenko, M. I., Chen, L.-W. A., Green, M. C., Watson, J. G., and Chow, J. C.:
890 Photoacoustic optical properties at UV, VIS, and near IR wavelengths for
891 laboratory generated and winter time ambient urban aerosols, *Atmos. Chem. Phys.*,
892 12, 2587–2601, <https://doi.org/10.5194/acp-12-2587-2012>, 2012.

893 Holben, B. N., Eck, T. F., Slutsker, I., Tanré, D., Buis, J. P., Setzer, A., Vermote, E.,
894 Reagan, J. A., Kaufman, Y. J., Nakajima, T., Lavenu, F., Jankowiak, I., and
895 Smirnov, A.: AERONET—A Federated Instrument Network and Data Archive for
896 Aerosol Characterization, *Remote Sensing of Environment*, 66, 1–16,
897 [https://doi.org/10.1016/S0034-4257\(98\)00031-5](https://doi.org/10.1016/S0034-4257(98)00031-5), 1998.

898 Intergovernmental Panel On Climate Change (Ipcc): *Climate Change 2021 – The*
899 *Physical Science Basis: Working Group I Contribution to the Sixth Assessment*
900 *Report of the Intergovernmental Panel on Climate Change*, 1st ed., Cambridge
901 University Press, <https://doi.org/10.1017/9781009157896>, 2023.

902 Kirchstetter, T. W., Novakov, T., and Hobbs, P. V.: Evidence that the spectral
903 dependence of light absorption by aerosols is affected by organic carbon, *J.*
904 *Geophys. Res.*, 109, 2004JD004999, <https://doi.org/10.1029/2004JD004999>,
905 2004.

906 Kok, J. F., Ridley, D. A., Zhou, Q., Miller, R. L., Zhao, C., Heald, C. L., Ward, D. S.,
907 Albani, S., and Haustein, K.: Smaller desert dust cooling effect estimated from
908 analysis of dust size and abundance, *Nature Geosci*, 10, 274–278,
909 <https://doi.org/10.1038/ngeo2912>, 2017.

910 Lack, D. A. and Cappa, C. D.: Impact of brown and clear carbon on light absorption
911 enhancement, single scatter albedo and absorption wavelength dependence of
912 black carbon, *Atmos. Chem. Phys.*, 10, 4207–4220, [https://doi.org/10.5194/acp-](https://doi.org/10.5194/acp-10-4207-2010)
913 [10-4207-2010](https://doi.org/10.5194/acp-10-4207-2010), 2010.

914 Lack, D. A. and Langridge, J. M.: On the attribution of black and brown carbon light
915 absorption using the Ångström exponent, *Atmos. Chem. Phys.*, 13, 10535–10543,
916 <https://doi.org/10.5194/acp-13-10535-2013>, 2013.

917 Laskin, A., Laskin, J., and Nizkorodov, S. A.: Chemistry of Atmospheric Brown Carbon,
918 *Chem. Rev.*, 115, 4335–4382, <https://doi.org/10.1021/cr5006167>, 2015.

919 Lee, L. A., Reddington, C. L., and Carslaw, K. S.: On the relationship between aerosol
920 model uncertainty and radiative forcing uncertainty, *Proc. Natl. Acad. Sci. U.S.A.*,
921 113, 5820–5827, <https://doi.org/10.1073/pnas.1507050113>, 2016.

922 Lewis, K., Arnott, W. P., Moosmüller, H., and Wold, C. E.: Strong spectral variation of
923 biomass smoke light absorption and single scattering albedo observed with a novel
924 dual-wavelength photoacoustic instrument, *J. Geophys. Res.*, 113, 2007JD009699,
925 <https://doi.org/10.1029/2007JD009699>, 2008.

926 Li, J., Liu, C., Yin, Y., and Kumar, K. R.: Numerical investigation on the Ångström

927 exponent of black carbon aerosol, *JGR Atmospheres*, 121, 3506–3518,
928 <https://doi.org/10.1002/2015JD024718>, 2016.

929 Li, J., Carlson, B. E., Yung, Y. L., Lv, D., Hansen, J., Penner, J. E., Liao, H.,
930 Ramaswamy, V., Kahn, R. A., Zhang, P., Dubovik, O., Ding, A., Lacis, A. A.,
931 Zhang, L., and Dong, Y.: Scattering and absorbing aerosols in the climate system,
932 *Nat Rev Earth Environ*, 3, 363–379, <https://doi.org/10.1038/s43017-022-00296-7>,
933 2022.

934 [Li, L., Dubovik, O., Derimian, Y., Schuster, G. L., Lapyonok, T., Litvinov, P., Ducos,](#)
935 [F., Fuertes, D., Chen, C., Li, Z., Lopatin, A., Torres, B., and Che, H.: Retrieval of](#)
936 [aerosol components directly from satellite and ground-based measurements,](#)
937 [Atmos. Chem. Phys., 19, 13409–13443, https://doi.org/10.5194/acp-19-13409-](#)
938 [2019, 2019.](#)

939 Li, W., Riemer, N., Xu, L., Wang, Y., Adachi, K., Shi, Z., Zhang, D., Zheng, Z., and
940 Laskin, A.: Microphysical properties of atmospheric soot and organic particles:
941 measurements, modeling, and impacts, *npj Clim Atmos Sci*, 7, 65,
942 <https://doi.org/10.1038/s41612-024-00610-8>, 2024.

943 Li, Y., Fu, T.-M., Yu, J. Z., Zhang, A., Yu, X., Ye, J., Zhu, L., Shen, H., Wang, C., Yang,
944 X., Tao, S., Chen, Q., Li, Y., Li, L., Che, H., and Heald, C. L.: Nitrogen dominates
945 global atmospheric organic aerosol absorption, *Science*, 387, 989–995,
946 <https://doi.org/10.1126/science.adr4473>, 2025.

947 Liu, C., Chung, C. E., Yin, Y., and Schnaiter, M.: The absorption Ångström exponent

948 of black carbon: from numerical aspects, *Atmos. Chem. Phys.*, 18, 6259–6273,
949 <https://doi.org/10.5194/acp-18-6259-2018>, 2018.

950 Malm, W. C., Sisler, J. F., Huffman, D., Eldred, R. A., and Cahill, T. A.: Spatial and
951 seasonal trends in particle concentration and optical extinction in the United States,
952 *J. Geophys. Res.*, 99, 1347–1370, <https://doi.org/10.1029/93JD02916>, 1994.

953 Moosmüller, H., Chakrabarty, R. K., Ehlers, K. M., and Arnott, W. P.: Absorption
954 Ångström coefficient, brown carbon, and aerosols: basic concepts, bulk matter,
955 and spherical particles, *Atmos. Chem. Phys.*, 11, 1217–1225,
956 <https://doi.org/10.5194/acp-11-1217-2011>, 2011.

957 Nishant, N., Sherwood, S. C., and Geoffroy, O.: Aerosol-induced modification of
958 organised convection and top-of-atmosphere radiation, *npj Clim Atmos Sci*, 2, 33,
959 <https://doi.org/10.1038/s41612-019-0089-1>, 2019.

960 Park, S., Son, S.-C., and Lee, S.: Characterization, sources, and light absorption of fine
961 organic aerosols during summer and winter at an urban site, *Atmospheric Research*,
962 213, 370–380, <https://doi.org/10.1016/j.atmosres.2018.06.017>, 2018.

963 Peng, K., Xin, J., Zhu, X., Wang, X., Cao, X., Ma, Y., Ren, X., Zhao, D., Cao, J., and
964 Wang, Z.: Machine learning model to accurately estimate the planetary boundary
965 layer height of Beijing urban area with ERA5 data, *Atmospheric Research*, 293,
966 106925, <https://doi.org/10.1016/j.atmosres.2023.106925>, 2023.

967 [Petzold, A., Ogren, J. A., Fiebig, M., Laj, P., Li, S.-M., Baltensperger, U., Holzer-Popp,](#)
968 [T., Kinne, S., Pappalardo, G., Sugimoto, N., Wehrli, C., Wiedensohler, A., and](#)

969 [Zhang, X.-Y.: Recommendations for reporting “black carbon” measurements,](#)
970 [Atmos. Chem. Phys., 13, 8365–8379, <https://doi.org/10.5194/acp-13-8365-2013>,](#)
971 [2013.](#)

972 Ponczek, M., Franco, M. A., Carbone, S., Rizzo, L. V., Monteiro Dos Santos, D., Morais,
973 F. G., Duarte, A., Barbosa, H. M. J., and Artaxo, P.: Linking the chemical
974 composition and optical properties of biomass burning aerosols in Amazonia,
975 Environ. Sci.: Atmos., 2, 252–269, <https://doi.org/10.1039/D1EA00055A>, 2022.

976 Russell, P. B., Bergstrom, R. W., Shinozuka, Y., Clarke, A. D., DeCarlo, P. F., Jimenez,
977 J. L., Livingston, J. M., Redemann, J., Dubovik, O., and Strawa, A.: Absorption
978 Angstrom Exponent in AERONET and related data as an indicator of aerosol
979 composition, Atmos. Chem. Phys., 10, 1155–1169, [https://doi.org/10.5194/acp-](https://doi.org/10.5194/acp-10-1155-2010)
980 [10-1155-2010](#), 2010.

981 ~~Samset, B. H., Stjern, C. W., Andrews, E., Kahn, R. A., Myhre, G., Schulz, M., and~~
982 ~~Schuster, G. L.: Aerosol Absorption: Progress Towards Global and Regional~~
983 ~~Constraints, Curr Clim Change Rep, 4, 65–83, [https://doi.org/10.1007/s40641-](https://doi.org/10.1007/s40641-018-0091-4)~~
984 ~~[018-0091-4](#), 2018.~~

985 Sand, M., Samset, B. H., Myhre, G., Glib, J., Bauer, S. E., Bian, H., Chin, M., Checa-
986 Garcia, R., Ginoux, P., Kipling, Z., Kirkevåg, A., Kokkola, H., Le Sager, P., Lund,
987 M. T., Matsui, H., Van Noije, T., Olivie, D. J. L., Remy, S., Schulz, M., Stier, P.,
988 Stjern, C. W., Takemura, T., Tsigaridis, K., Tsyro, S. G., and Watson-Parris, D.:
989 Aerosol absorption in global models from AeroCom phase III, Atmos. Chem.

990 Phys., 21, 15929–15947, <https://doi.org/10.5194/acp-21-15929-2021>, 2021.

991 Scarnato, B. V., Vahidinia, S., Richard, D. T., and Kirchstetter, T. W.: Effects of internal
992 mixing and aggregate morphology on optical properties of black carbon using a
993 discrete dipole approximation model, *Atmos. Chem. Phys.*, 13, 5089–5101,
994 <https://doi.org/10.5194/acp-13-5089-2013>, 2013.

995 Schuster, G. L., Dubovik, O., and Arola, A.: Remote sensing of soot carbon – Part 1:
996 Distinguishing different absorbing aerosol species, *Atmos. Chem. Phys.*, 16,
997 1565–1585, <https://doi.org/10.5194/acp-16-1565-2016>, 2016a.

998 Schuster, G. L., Dubovik, O., Arola, A., Eck, T. F., and Holben, B. N.: Remote sensing
999 of soot carbon – Part 2: Understanding the absorption Ångström exponent, *Atmos.*
1000 *Chem. Phys.*, 16, 1587–1602, <https://doi.org/10.5194/acp-16-1587-2016>, 2016b.

1001 [Seinfeld, J. H., and Pandis, S. N.: *Atmospheric Chemistry and Physics: From Air*](#)
1002 [Pollution to Climate Change, Wiley, 2016.](#)

1003 Shang, D., Hu, M., Zheng, J., Qin, Y., Du, Z., Li, M., Fang, J., Peng, J., Wu, Y., Lu, S.,
1004 and Guo, S.: Particle number size distribution and new particle formation under
1005 the influence of biomass burning at a high altitude background site at Mt. Yulong
1006 (3410 m), China, *Atmos. Chem. Phys.*, 18, 15687–15703,
1007 <https://doi.org/10.5194/acp-18-15687-2018>, 2018.

1008 Sinyuk, A., Holben, B. N., Eck, T. F., Giles, D. M., Slutsker, I., Korkin, S., Schafer, J.
1009 S., Smirnov, A., Sorokin, M., and Lyapustin, A.: The AERONET Version 3 aerosol
1010 retrieval algorithm, associated uncertainties and comparisons to Version 2, *Atmos.*

1011 Meas. Tech., 13, 3375–3411, <https://doi.org/10.5194/amt-13-3375-2020>, 2020.

1012 Sotiropoulou, R. E. P., Kaskaoutis, D. G., Kalkavouras, P., Grivas, G., Petrinoli, K.,
1013 Garas, S. K., Liakakou, E., Tagaris, E., and Mihalopoulos, N.: Spatial variability
1014 of carbonaceous aerosols and absorption characteristics between urban
1015 background and residential sites during wintertime at a major Mediterranean city
1016 (Athens; Greece), Atmospheric Research, 323, 108163,
1017 <https://doi.org/10.1016/j.atmosres.2025.108163>, 2025.

1018 Tao, C., Peng, Y., Zhang, Q., Zhang, Y., Gong, B., Wang, Q., and Wang, W.: Diagnosing
1019 ozone–NO_x–VOC–aerosol sensitivity and uncovering causes of urban–
1020 nonurban discrepancies in Shandong, China, using transformer-based estimations,
1021 Atmos. Chem. Phys., 24, 4177–4192, <https://doi.org/10.5194/acp-24-4177-2024>,
1022 2024.

1023 Tian, J., Wang, Q., Ni, H., Wang, M., Zhou, Y., Han, Y., Shen, Z., Pongpiachan, S.,
1024 Zhang, N., Zhao, Z., Zhang, Q., Zhang, Y., Long, X., and Cao, J.: Emission
1025 Characteristics of Primary Brown Carbon Absorption From Biomass and Coal
1026 Burning: Development of an Optical Emission Inventory for China, JGR
1027 Atmospheres, 124, 1879–1893, <https://doi.org/10.1029/2018JD029352>, 2019.

1028 Tian, P., Zhang, L., Ma, J., Tang, K., Xu, L., Wang, Y., Cao, X., Liang, J., Ji, Y., Jiang,
1029 J. H., Yung, Y. L., and Zhang, R.: Radiative absorption enhancement of dust mixed
1030 with anthropogenic pollution over East Asia, Atmos. Chem. Phys., 18, 7815–7825,
1031 <https://doi.org/10.5194/acp-18-7815-2018>, 2018.

1032 Tian, P., Zhang, N., Li, J., Fan, X., Guan, X., Lu, Y., Shi, J., Chang, Y., and Zhang, L.:
1033 Potential influence of fine aerosol chemistry on the optical properties in a semi-
1034 arid region, *Environmental Research*, 216, 114678,
1035 <https://doi.org/10.1016/j.envres.2022.114678>, 2023.

1036 Truex, T. J. and Anderson, J. E.: Mass monitoring of carbonaceous aerosols with a
1037 spectrophone, *Atmospheric Environment* (1967), 13, 507–509,
1038 [https://doi.org/10.1016/0004-6981\(79\)90143-4](https://doi.org/10.1016/0004-6981(79)90143-4), 1979.

1039 Utry, N., Ajtai, T., Filep, Á., Pintér, M., Török, Zs., Bozóki, Z., and Szabó, G.:
1040 Correlations between absorption Angström exponent (AAE) of wintertime
1041 ambient urban aerosol and its physical and chemical properties, *Atmospheric*
1042 *Environment*, 91, 52–59, <https://doi.org/10.1016/j.atmosenv.2014.03.047>, 2014.

1043 [Wang, L., Li, Z., Tian, Q., Ma, Y., Zhang, F., Zhang, Y., Li, D., Li, K., and Li, L.:](#)
1044 [Estimate of aerosol absorbing components of black carbon, brown carbon, and](#)
1045 [dust from ground-based remote sensing data of sun-sky radiometers. *JGR*](#)
1046 [Atmospheres](#), 118, 6534–6543, <https://doi.org/10.1002/jgrd.50356>, 2013.

1047 Wang, N., Wang, Y., Lu, C., Zhu, B., Yan, X., Sun, Y., Xu, J., Zhang, J., and Shen, Z.:
1048 Interpretable ensemble learning unveils main aerosol optical properties in
1049 predicting cloud condensation nuclei number concentration, *npj Clim Atmos Sci*,
1050 8, 302, <https://doi.org/10.1038/s41612-025-01181-y>, 2025a.

1051 Wang, Q., Ye, J., Wang, Y., Zhang, T., Ran, W., Wu, Y., Tian, J., Li, L., Zhou, Y., Hang
1052 Ho, S. S., Dang, B., Zhang, Q., Zhang, R., Chen, Y., Zhu, C., and Cao, J.:

1053 Wintertime Optical Properties of Primary and Secondary Brown Carbon at a
1054 Regional Site in the North China Plain, *Environ. Sci. Technol.*, 53, 12389–12397,
1055 <https://doi.org/10.1021/acs.est.9b03406>, 2019.

1056 Wang, Q., Liu, H., Ye, J., Tian, J., Zhang, T., Zhang, Y., Liu, S., and Cao, J.: Estimating
1057 Absorption Ångström Exponent of Black Carbon Aerosol by Coupling
1058 Multiwavelength Absorption with Chemical Composition, *Environ. Sci. Technol.*
1059 *Lett.*, 8, 121–127, <https://doi.org/10.1021/acs.estlett.0c00829>, 2021.

1060 Wang, W., Tian, P., and Wu, Y.: Interpretable Machine Learning Quantifies
1061 Composition and Size Controls on Aerosol Spectral Absorption,
1062 <https://doi.org/10.5281/ZENODO.17852818>, 2025b.

1063 Wang, Y., Huang, R.-J., Zhong, H., Wang, T., Yang, L., Yuan, W., Xu, W., and An, Z.:
1064 Predictions of the Optical Properties of Brown Carbon Aerosol by Machine
1065 Learning with Typical Chromophores, *Environ. Sci. Technol.*, 58, 20588–20597,
1066 <https://doi.org/10.1021/acs.est.4c09031>, 2024.

1067 Wu, Y., Yan, P., Tian, P., Tao, J., Li, L., Chen, J., Zhang, Y., Cao, N., Chen, C., and
1068 Zhang, R.: Spectral Light Absorption of Ambient Aerosols in Urban Beijing during
1069 Summer: An Intercomparison of Measurements from a Range of Instruments,
1070 *Aerosol Air Qual. Res.*, 15, 1178–1187, <https://doi.org/10.4209/aaqr.2014.09.0224>,
1071 2015.

1072 Yan, C., Zheng, M., Bosch, C., Andersson, A., Desyaterik, Y., Sullivan, A. P., Collett, J.
1073 L., Zhao, B., Wang, S., He, K., and Gustafsson, Ö.: Important fossil source

1074 contribution to brown carbon in Beijing during winter, *Sci Rep*, 7, 43182,
1075 <https://doi.org/10.1038/srep43182>, 2017.

1076 Yang, Z., Wang, Q., Wang, Q., Ma, N., Tian, J., Zhou, Y., Xu, G., Gao, M., Zhou, X.,
1077 Zhang, Y., Ran, W., Yang, N., Tao, J., Hong, J., Wu, Y., Cao, J., Su, H., and Cheng,
1078 Y.: Laboratory studies on the optical, physical, and chemical properties of fresh
1079 and aged biomass burning aerosols, <https://doi.org/10.5194/egusphere-2025-1020>,
1080 25 April 2025.

1081 [Zhang, X., Li, L., Chen, C., Zheng, Y., Dubovik, O., Derimian, Y., Lopatin, A., Gui, K.,](#)
1082 [Wang, Y., Zhao, H., Liang, Y., Holben, B., Che, H., and Zhang, X.: Extensive](#)
1083 [characterization of aerosol optical properties and chemical component](#)
1084 [concentrations: Application of the GRASP/Component approach to long-term](#)
1085 [AERONET measurements, *Science of The Total Environment*, 812, 152553,](#)
1086 <https://doi.org/10.1016/j.scitotenv.2021.152553>, 2022.

1087 Zhang, X., Mao, M., Yin, Y., and Tang, S.: The absorption Ångstrom exponent of black
1088 carbon with brown coatings: effects of aerosol microphysics and parameterization,
1089 *Atmos. Chem. Phys.*, 20, 9701–9711, <https://doi.org/10.5194/acp-20-9701-2020>,
1090 2020.

1091 Zhang, X., Li, L., Che, H., Dubovik, O., Derimian, Y., Holben, B., Gupta, P., Eck, T. F.,
1092 Lind, E. S., Toledano, C., Xia, X., Zheng, Y., Gui, K., and Zhang, X.: Aerosol
1093 Components Derived from Global AERONET Measurements by GRASP: A New
1094 Value-Added Aerosol Component Global Dataset and Its Application, *Bulletin of*

1095 the American Meteorological Society, 105, E1822–E1848,
1096 <https://doi.org/10.1175/BAMS-D-23-0260.1>, 2024.

1097 Zhang, Z., Wang, Y., Chen, X., Xu, L., Zheng, Z., Ching, J., Zhu, S., Liu, D., and Li,
1098 W.: Absorption enhancement and shielding effect of brown organic coating on
1099 black carbon aerosols, *npj Clim Atmos Sci*, 8, 102,
1100 <https://doi.org/10.1038/s41612-025-00989-y>, 2025.

1101 Zhao, S., Hu, B., Du, C., Tang, L., Ma, Y., Liu, H., Zou, J., Liu, Z., Wei, J., and Wang,
1102 Y.: Aerosol optical characteristics and radiative forcing in urban Beijing,
1103 *Atmospheric Environment*, 212, 41–53,
1104 <https://doi.org/10.1016/j.atmosenv.2019.05.034>, 2019.

1105